INTERNATIONAL JOURNAL FOR NUMERICAL METHODS IN ENGINEERING
Int. J. Numer. Meth. Engng (2011)
Published online in Wiley Online Library (wileyonlinelibrary.com). DOI: 10.1002/nme.3114

Delamination analysis of composites by new orthotropic bimaterial extended finite element method

S. Esna Ashari and S. Mohammadi*, †

School of Civil Engineering, University of Tehran, Tehran, Iran

SUMMARY

The extended finite element method (XFEM) is further improved for fracture analysis of composite laminates containing interlaminar delaminations. New set of bimaterial orthotropic enrichment functions are developed and utilized in XFEM analysis of linear-elastic fracture mechanics of layered composites. Interlaminar crack-tip enrichment functions are derived from analytical asymptotic displacement fields around a traction-free interfacial crack. Also, heaviside and weak discontinuity enrichment functions are utilized in modeling discontinuous fields across interface cracks and bimaterial weak discontinuities, respectively. In this procedure, elements containing a crack-tip or strong/weak discontinuities are not required to conform to those geometries. In addition, the same mesh can be used to analyze different interlaminar cracks or delamination propagation. The domain interaction integral approach is also adopted in order to numerically evaluate the mixed-mode stress intensity factors. A number of benchmark tests are simulated to assess the performance of the proposed approach and the results are compared with available reference results. Copyright © 2011 John Wiley & Sons, Ltd.

Received 2 March 2010; Revised 6 October 2010; Accepted 6 December 2010

KEY WORDS: extended finite element method (XFEM); delamination; orthotropic composites; enrichment functions; weak discontinuity; interlaminar crack

1. INTRODUCTION

Design of composite materials requires prediction of their structural performances in the presence of any form of potential damage such as manufacturing flaws and inhomogeneities, fiber breakage, matrix cracking, and delamination. Interface cracking, also known as interlaminar debonding or delamination, is one of the most commonly encountered failure modes in composite laminates and can cause severe performance and safety problems, such as stiffness and load bearing capacity reduction and even structural disintegrity. Therefore, it is of paramount importance to study delamination in laminated composites in order to accurately assess and/or predict the behavior of laminates.

Delamination can be formed in different stages of the life of a laminar composite, such as manufacture, transportation, setup, and service. Delaminations can b e originated from geometrical effects such as curved sections, sudden changes of cross sections, and in free edges. In addition to temperature and moisture effects, it can also be initiated during manufacturing stages as a result of matrix shrinkage. Impact is another important source of delamination in composite structures that causes internal damages in the interface of two adjacent plies.

*Correspondence to: S. Mohammadi, High Performance Computing Lab, School of Civil Engineering, University of Tehran, Tehran, Iran.
†E-mail: smoham@ut.ac.ir

Many analytical investigations have been devoted to delamination analysis. Williams [1] discovered the oscillatory near-tip behavior for a traction-free interface crack between two dissimilar isotropic elastic materials. England [2], Erdogan [3], Rice and Sih [4], Malysev and Salganik [5], Comninou [6], Comninou and Schmuser [7], Sun and Jih [8], Hutchinson *et al.* [9] and Rice [10] obtained further results on this kind of problem, reporting similar oscillatory nature of the near crack-tip (interlaminar) displacement fields. England [2] was the first who predicted interpenetration or overlapping of the crack surfaces, which was a violation of the basic 'open-crack' assumption; implying the existence of a contact zone near the crack-tip. Erdogan [3] and Rice and Sih [4] adopted the Griffith–Irwin fracture theory to obtain expressions for the bimaterial stress intensity factors (SIFs) K_1 and K_2, which were not associated, as in the homogeneous case, with the opening and shearing modes of fracture, respectively.

Comninou [6] and Comninou and Schmuser [7] studied the stress singularities' behavior near the tip of an interfacial crack by assuming that the crack was not completely open and its surfaces were in contact near the tip. Also, Sun and Jih [8] discussed the strain energy release rates for an interfacial crack between isotropic solids, and found that the individual mode I (G_1) and mode II (G_2) strain energy release rates did not exist due to their oscillatory natures, although the total strain energy release rate was well-defined.

The interface crack between two anisotropic materials have been studied by Gotoh [11], Clements [12], Willis [13], Wang and Choi [14, 15], Ting [16], Tewary [17], Bassani and Qu [18], Sun and Manoharan [19], Wu [20], Gao *et al.* [21] and Hwu [22, 23], among the others. Several basic crack problems were solved, with an emphasize on calculation of the oscillatory index. Willis [13], for example, defined a stress concentration vector, which involved three complex or six real quantities. Wang and Choi [14, 15] studied the interfacial crack behavior in anisotropic composites under mixed-mode loadings using a partially closed interface crack model. Ting [16] studied the dependence of this oscillatory phenomenon on the orientation of the two materials. Bassani and Qu [18] made a breakthrough by considering bimaterials with no pathological behavior at interface crack-tips. They proved a necessary and sufficient non-oscillatory condition, under which they could define the three modes separately and found that the Irwin-type energy release rate expression was simply the average of the corresponding results for the two homogeneous materials. Sun and Manoharan [19] discussed the strain energy release rates for an interfacial crack between two orthotropic solids subjected to tensile and shear tractions.

Hwu [23], Suo [24], Qian and Sun [25], Hemanth *et al.* [26], Yang *et al.* [27], and Lee [28] extended the results of previously available studies for an interface crack between two anisotropic materials to an interfacial crack between two orthotropic materials.

From the computational point of view, there are many numerical methods for analyzing orthotropic composites, including the boundary element method (BEM), the finite element method (FEM), the finite difference method (FDM), and meshless methods such as the element-free Galerkin method (EFG). Crack simulation in FEM has been performed by a number of methods such as the continuous smeared crack model and several discontinuous approaches such as the discrete inter-element crack model, the discrete crack model, and the discrete element-based model [29]. Although the finite element method is capable of analysis of non-linear systems and can be easily adapted to general boundary conditions and complex geometries, the elements associated with cracks must conform to crack faces and remeshing techniques are then required to simulate the crack propagation.

A natural extension, the extended finite element method (XFEM), is specifically designed to enhance the conventional FEM in order to solve problems that exhibit strong and weak discontinuities in material and geometric behavior, while preserving the finite element original advantages. The basis of this method was originally proposed by Belytschko and Black [30], combining the FEM with the concept of partition of unity to improve the FEM deficiencies in modeling discontinuities. In XFEM, elements around a crack are enriched with a discontinuous function and near-tip asymptotic displacement fields. The major advantage of this method is that the mesh is prepared independent of the existence of any discontinuities. As a result, XFEM can substantially simplify

DOI: 10.1002/nme

the modeling of a cracked continuum and hence can be used to perform effective stress analyses related to fracture mechanics.

This method was improved by Möes *et al.* [31] to its present form and further developed by Sukumar *et al.* [32]: extending the method to three dimensional domain; Dolbow *et al.* [33]: solving frictional contact problems; Mergheim *et al.* [34]: simulation of cohesive cracks; Belytschko *et al.* [35] and Belytschko and Chen [36]: modeling dynamic crack propagation for isotropic materials; Rozycki *et al.* [37]: introducing methods to alleviate mesh constraints on internal or external boundaries; and Bechet *et al.* [38]: discussing on improved implementation and robustness study of XFEM for stress analysis around cracks.

Asadpoure *et al.* [39, 40], Asadpoure and Mohammadi [41] and Mohammadi [29] have extended the method to orthotropic media by deriving new set of orthotropic enrichment functions. They developed three different sets of enrichment functions for various types of composites based on available analytical solutions. Recently, Motamedi and Mohammadi [42, 43] further extended the method to dynamic analysis of stationary and propagating cracks in orthotropic media and proposed new time-independent moving orthotropic enrichment functions for dynamic analysis of composites [44].

In earlier simulations of interlaminar cracks, continuum elasticity [45–47], interface elements [48], and contact-based finite/discrete element methodology [49, 50] were used to analyze partially delaminated layered composites. Later, Sukumar *et al.* [51] developed partition of unity-based enrichment techniques for bimaterial interface cracks between two isotropic media, while Hettich and Ramm [52] studied the Interface material failure and Remmers *et al.* [53] presented a partition of unity finite element based on a solid-like shell element for simulation of delamination growth in thin-layered structures. The delamination crack was incorporated in the element as a jump in the displacement field, while no crack-tip enrichment was assumed. Also, Hettich *et al.* [54] reported modeling of failure in composites by XFEM and level sets within a multiscale framework.

Recently, Nagashima and Suemasu [55, 56] applied XFEM to stress analyses of structures containing interface cracks between dissimilar isotropic materials and also modeled interlaminar delaminations of composite laminates by the near-tip functions for homogeneous isotropic cracks in order to examine the behavior of orthotropic composite materials. They concluded that the near-tip functions for isotropic cracks cannot represent the asymptotic displacement solution for a crack in an orthotropic material and near-tip functions for orthotropic materials should be developed.

In this research, XFEM is adopted and further improved for modeling interfacial cracks between two orthotropic media by a new set of bimaterial orthotropic enrichment functions, completing the earlier research proposed by Esna Ashari and Mohammadi [57, 58]. The new interlaminar crack-tip enrichment functions are derived from analytical asymptotic displacement fields around a traction-free interfacial crack. Combined mode I and mode II loading conditions are studied and mixed-mode SIFs are numerically evaluated to determine fracture properties of a problem using the domain form of the contour interaction integral. In order to examine the performance of the proposed approach, various numerical examples are simulated and the results are compared with reference solutions. The new enrichments are expected to allow for full XFEM fracture analysis of layered orthotropic composites including both layer crackings and interlaminar debondings, which is the subject of future studies.

2. FRACTURE MECHANICS

2.1. Fracture mechanics for 2D orthotropic materials

The stress–strain law in an arbitrary 2D linear-elastic plane stress material can be written in the following compact form [59]:

$$\varepsilon_\alpha = a_{\alpha\beta}\sigma_\beta \quad (\alpha, \beta = 1, 2, 6) \tag{1}$$

DOI: 10.1002/nme

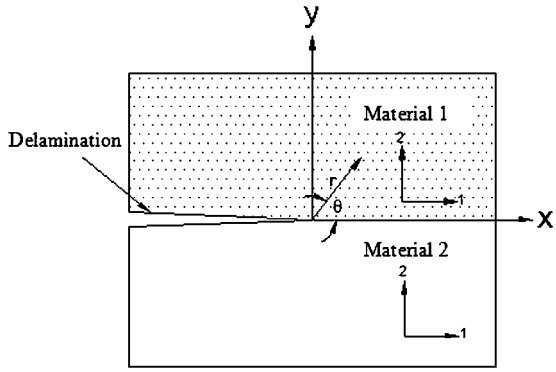

Figure 1. Interface crack between two orthotropic materials.

with

$$\begin{aligned} \varepsilon_1 &= \varepsilon_{11}, \quad \varepsilon_2 = \varepsilon_{22}, \quad \varepsilon_6 = 2\varepsilon_{12} \\ \sigma_1 &= \sigma_{11}, \quad \sigma_2 = \sigma_{22}, \quad \sigma_6 = \sigma_{12} \end{aligned} \tag{2}$$

and

$$\begin{aligned} a_{11} &= S_{1111}, \quad a_{12} = S_{1122}, \quad a_{16} = 2S_{1112} \\ a_{21} &= S_{2211}, \quad a_{22} = S_{2222}, \quad a_{26} = 2S_{2212} \\ a_{61} &= 2S_{1211}, \quad a_{62} = 2S_{1222}, \quad a_{66} = 4S_{1212} \end{aligned} \tag{3}$$

where ε_{ij} and σ_{kl} are linear strain and stress tensors, respectively, and S_{ijkl} is the compliance tensor $\varepsilon_{ij} = S_{ijkl}\sigma_{kl}$ $(i, j, k, l = 1, 2)$.

For a plane strain state, parameters a_{ij} are replaced by b_{ij}

$$b_{ij} = a_{ij} - \frac{a_{i3} - a_{3i}}{a_{33}} \quad (i, j = 1, 2, 6) \tag{4}$$

2.2. *Fracture mechanics for orthotropic bimaterial interfaces*

A traction-free interface crack between two dissimilar orthotropic materials is considered. The crack is located in (x, y) plane and (r, θ) are the local polar coordinates defined on the crack-tip, as shown in Figure 1. The elastic principal directions are assumed to be defined normal to or parallel with the crack direction in both materials.

According to Lee *et al.* [60], the governing equilibrium, elastic constitutive law, and compatibility equations can be combined into a partial differential equation with the following characteristic equation in terms of a complex variable $z = x + my$,

$$m^4 + 2B_{12}m^2 + K_{66} = 0 \tag{5}$$

where

$$B_{12} = \frac{1}{2}\frac{(2a_{12} + a_{66})}{a_{11}}, \quad K_{66} = \frac{a_{22}}{a_{11}} \tag{6}$$

The characteristic roots of Equation (5) (m_l and m_s) are purely imaginary when $\sqrt{K_{66}} < B_{12}$; $K_{66} > 0$ or complex when $\sqrt{K_{66}} > |B_{12}|$; $K_{66} > 0$, known as type 1 and type 2, respectively. Most orthotropic materials are categorized as type 1 and their conjugated roots are:

$$m_l = ip, \quad m_s = iq \tag{7}$$

DOI: 10.1002/nme

where

$$p=\sqrt{B_{12}-\sqrt{B_{12}^2-K_{66}}} \tag{8}$$

$$q=\sqrt{B_{12}+\sqrt{B_{12}^2-K_{66}}} \tag{9}$$

The analytical solutions for two-dimensional asymptotic displacement and stress fields around a traction-free interfacial crack-tip were previously obtained by Lee [28]. They are defined in detail in Appendix A and can be expressed in the following general form:

$$u_i=\sum_{j=1}^{8}\{K_{\mathrm{I}}A_jF_j(r,\theta)+K_{\mathrm{II}}B_jF_j(r,\theta)\},\quad i=x,y \tag{10}$$

where K_{I} and K_{II} are the mode 1 and 2 SIFs, respectively, and A_j, B_j are spatially independent functions of the roots p, q, coefficients a_{ij} and the oscillation index ε defined as

$$\varepsilon=\frac{1}{2\pi}\ln\left(\frac{1-\beta}{1+\beta}\right) \tag{11}$$

where β is the second Dundurs parameter [61] defined in Appendix A. All necessary parameters are defined in Appendix A. Functions $F_j(r,\theta)$ exclusively define the nature of the displacement fields [58]. They can be defined in the following compact form:

$$\{F_j(r,\theta)\}_{j=1}^{8}=\left\{e^{\mu\varepsilon\theta_z}S_j\left(\varepsilon\ln(r_z)-\mu\frac{\theta_z}{2}\right)\sqrt{r_z}\right\}_{j=1}^{8}$$

$$S_j()=\begin{cases}\cos(), & j=1,3,5,7,\\ \sin(), & j=2,4,6,8,\end{cases}\quad z=\begin{cases}l & j=1-4,\\ s & j=5-8,\end{cases}\quad \mu=\begin{cases}1 & j=3,4,7,8\\ -1 & j=1,2,5,6\end{cases} \tag{12}$$

where $r_z, \theta_z(z=l,s)$ are related to polar coordinate system (r,θ) as

$$\begin{aligned} r_z&=r\sqrt{\cos^2\theta+Z_z^2\sin^2\theta},\\ \theta_z&=\tan^{-1}(Z_z\tan\theta),\end{aligned}\quad z=l,s,\begin{cases}Z_l=p\\ Z_s=q\end{cases} \tag{13}$$

Equation (12) will be used to derive the new XFEM enrichment functions for reproduction of the singular orthotropic bimaterial interlaminar crack-tip stress fields.

3. EXTENDED FINITE ELEMENT METHOD

The XFEM is a way to facilitate modeling strong and weak discontinuities within finite elements by enriching the classical finite element displacement approximation using the framework of partition of unity. A literature review of related XFEM studies was given in Section 1.

3.1. Basic equations

A discontinuity in a domain, discretized by a number of finite elements with N nodes, is considered. In the XFEM, the displacement field for a point $\boldsymbol{x}$ inside the domain is approximated by [30]:

$$\boldsymbol{u}^h(\boldsymbol{x})=\sum_{\substack{I\\ n_I\in N}}\phi_I(\boldsymbol{x})\boldsymbol{u}_I+\sum_{\substack{J\\ n_J\in Ng}}\phi_J(\boldsymbol{x})\psi(\boldsymbol{x})\boldsymbol{a}_J \tag{14}$$

DOI: 10.1002/nme

where n_I is the node I, ϕ_I is the finite element shape function associated with node I, $\boldsymbol{u}_I$ is the vector of regular degrees of nodal freedom in the FEM, $\boldsymbol{a}_J$ is the added set of degrees of freedom to the standard finite element model, N^g is the set of nodes that the discontinuity is in its influence (support) domain, and $\psi(\boldsymbol{x})$ is the enrichment function.

3.2. Interface crack modeling

In order to model crack surfaces and crack-tips in the XFEM, the approximate displacement function $\boldsymbol{u}^h$ can be expressed as:

$$\boldsymbol{u}^h(\boldsymbol{x}) = \sum_{\substack{I \\ n_I \in N}} \phi_I(\boldsymbol{x})\boldsymbol{u}_I + \sum_{\substack{J \\ n_J \in N^H}} \boldsymbol{a}_J \phi_J(\boldsymbol{x}) H(\boldsymbol{x}) + \sum_{\substack{k \\ n_k \in N^F}} \phi_k(\boldsymbol{x}) \left(\sum_l \boldsymbol{b}_k^l F_l(\boldsymbol{x}) \right) + \sum_{\substack{r \\ n_r = N^\chi}} \boldsymbol{c}_r \phi_r(\boldsymbol{x}) \chi_r(\boldsymbol{x}) \tag{15}$$

where N^H is the set of nodes that have crack face (but not crack-tip) in their support domain, $\boldsymbol{a}_J$ is the vector of additional degrees of nodal freedom and is applied in modeling crack faces (not crack-tips), $H(\boldsymbol{x})$ is the heaviside function, N^F is the set of nodes associated with the crack-tip in its influence domain, $\boldsymbol{b}_k^l$ is the vector of additional degrees of nodal freedom for modeling crack-tips, $F_l(\boldsymbol{x})$ are crack-tip enrichment functions, N^χ is the set of nodes that have weak discontinuity, $\boldsymbol{c}_r$ is the vector of additional degrees of nodal freedom for modeling weak discontinuity interfaces, and $\chi_r(\boldsymbol{x})$ is the enrichment function used for modeling weak discontinuities.

In Equation (15), the first term is the classical finite element approximation, the second term is the enriched approximation related to crack surfaces, the third term is the enriched approximation for modeling crack-tips, while the last part is the enriched approximation used for modeling weak discontinuities. These three types of enriched nodes in a finite element modeling of an interface crack are depicted in Figure 2. Other nodes and their associated classical finite element degrees of freedom are not affected by the presence of the crack.

A simple shifting procedure on H and F in Equation (15) guarantees the interpolation [29]:

$$\boldsymbol{u}^h(\boldsymbol{x}) = \sum_{\substack{I \\ n_I \in N}} \phi_I(\boldsymbol{x})\boldsymbol{u}_I + \sum_{\substack{J \\ n_J \in N^H}} \boldsymbol{a}_J \phi_J(\boldsymbol{x})(H(\boldsymbol{x}) - H(\boldsymbol{x}_j)) + \sum_{\substack{k \\ n_k \in N^F}} \phi_k(\boldsymbol{x}) \left(\sum_l \boldsymbol{b}_k^l (F_l(\boldsymbol{x}) - F_l(\boldsymbol{x}_k)) \right)$$
$$+ \sum_{\substack{r \\ n_r = N^\chi}} \boldsymbol{c}_r \phi_r(\boldsymbol{x}) \chi_r(\boldsymbol{x}) \tag{16}$$

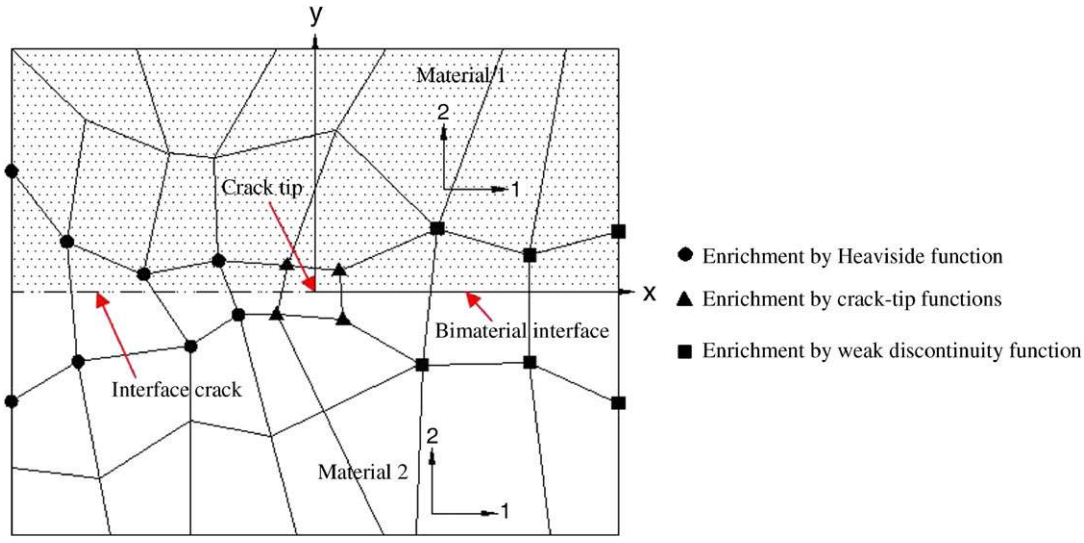

Figure 2. Node selection for enrichment; nodes enriched with crack-tip, heaviside, and weak discontinuity functions are marked by triangles, circles, and squares, respectively [58].

DOI: 10.1002/nme

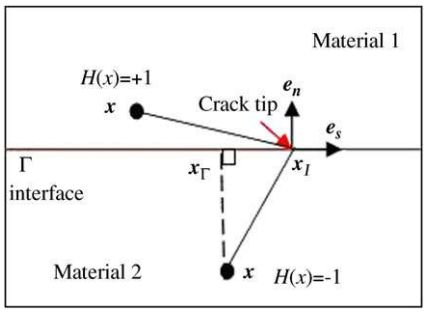

Figure 3. Normal and tangential unit vectors and definition of $H(x)$.

3.2.1. Crack length modeling. In Equation (15), $H(\boldsymbol{x})$ is the generalized heaviside function used to represent the discontinuity of displacement across a crack and takes the value $+1$ if the point $\boldsymbol{x}$ is above the crack and -1, otherwise [29].

$$H(\boldsymbol{x}) = \begin{cases} +1 & \text{if } (\boldsymbol{x}-\boldsymbol{x}_I).\boldsymbol{e_n} > 0 \\ -1 & \text{otherwise} \end{cases} \tag{17}$$

where $\boldsymbol{e_n}$ is the unit vector normal to the crack faces, $\mathbf{e_s} \times \mathbf{e_n} = \mathbf{e_z}$, $\mathbf{e_s}$ is the unit tangential vector, and $\boldsymbol{x}_I$ is the crack-tip point (Figure 3).

3.2.2. Orthotropic interface enrichments. In order to enhance the accuracy of approximation around an orthotropic bimaterial interface crack-tip, the following asymptotic crack-tip functions are extracted from the general crack-tip displacement fields (already defined in a compact form (12)):

$$\begin{aligned} \{F_l(r,\theta)\}_{l=1}^{8} = \Bigg[& \mathrm{e}^{-\varepsilon\theta_l}\cos\left(\varepsilon\ln(r_l)+\frac{\theta_l}{2}\right)\sqrt{r_l},\ \mathrm{e}^{-\varepsilon\theta_l}\sin\left(\varepsilon\ln(r_l)+\frac{\theta_l}{2}\right)\sqrt{r_l}, \\ & \mathrm{e}^{\varepsilon\theta_l}\cos\left(\varepsilon\ln(r_l)-\frac{\theta_l}{2}\right)\sqrt{r_l},\ \mathrm{e}^{\varepsilon\theta_l}\sin\left(\varepsilon\ln(r_l)-\frac{\theta_l}{2}\right)\sqrt{r_l}, \\ & \mathrm{e}^{-\varepsilon\theta_s}\cos\left(\varepsilon\ln(r_s)+\frac{\theta_s}{2}\right)\sqrt{r_s},\ \mathrm{e}^{-\varepsilon\theta_s}\sin\left(\varepsilon\ln(r_s)+\frac{\theta_s}{2}\right)\sqrt{r_s}, \\ & \mathrm{e}^{\varepsilon\theta_s}\cos\left(\varepsilon\ln(r_s)-\frac{\theta_s}{2}\right)\sqrt{r_s},\ \mathrm{e}^{\varepsilon\theta_s}\sin\left(\varepsilon\ln(r_s)-\frac{\theta_s}{2}\right)\sqrt{r_s}\Bigg] \end{aligned} \tag{18}$$

with

$$\begin{aligned} & r_j = r\sqrt{\cos^2\theta + Z_j^2\sin^2\theta}, \\ & \theta_j = \tan^{-1}(Z_j\tan\theta), \end{aligned} \quad j = l,s, \quad \begin{cases} Z_l = p \\ Z_s = q \end{cases} \tag{19}$$

where all parameters have been defined in Section 2.2 and Appendix A. These enrichment functions span the analytical asymptotic displacement fields for a traction-free interfacial crack.

It is worth noting that these sets of functions (apparently eight sets) contain combined typical terms of $\sqrt{r_j}\cos(\theta_j/2)$ or $\sqrt{r}[\cos^2\theta_j + Z^2\sin^2\theta_j]^{1/4}\cos(\theta_j/2)$. These include all generalized terms of $\sin\theta_j$, $\sin\theta_j\sin(\theta_j/2)$, $\sin\theta_j\cos(\theta_j/2)$, etc. and may generally span all various components of orthotropic material and isotropic bi-material enrichment functions.

DOI: 10.1002/nme

Enrichment functions (18) can be considered as an orthotropic extension to existing isotropic bimaterial enrichment functions, developed by Sukumar *et al.* [51],

$$
\begin{aligned}
[F_l^j(\boldsymbol{x})]_{j=1,2} = \Bigg\{ & \sqrt{r}\cos(\omega\log r)\mathrm{e}^{-\omega\theta}\sin\frac{\theta}{2}, \sqrt{r}\cos(\omega\log r)\mathrm{e}^{-\omega\theta}\cos\frac{\theta}{2}, \\
& \sqrt{r}\cos(\omega\log r)\mathrm{e}^{\omega\theta}\sin\frac{\theta}{2}, \sqrt{r}\cos(\omega\log r)\mathrm{e}^{\omega\theta}\cos\frac{\theta}{2}, \\
& \sqrt{r}\sin(\omega\log r)\mathrm{e}^{-\omega\theta}\sin\frac{\theta}{2}, \sqrt{r}\sin(\omega\log r)\mathrm{e}^{-\omega\theta}\cos\frac{\theta}{2}, \\
& \sqrt{r}\sin(\omega\log r)\mathrm{e}^{\omega\theta}\sin\frac{\theta}{2}, \sqrt{r}\sin(\omega\log r)\mathrm{e}^{\omega\theta}\cos\frac{\theta}{2}, \\
& \sqrt{r}\cos(\omega\log r)\mathrm{e}^{\omega\theta}\sin\frac{\theta}{2}\sin\theta, \sqrt{r}\cos(\omega\log r)\mathrm{e}^{\omega\theta}\cos\frac{\theta}{2}\sin\theta, \\
& \sqrt{r}\sin(\omega\log r)\mathrm{e}^{\omega\theta}\sin\frac{\theta}{2}\sin\theta, \sqrt{r}\sin(\omega\log r)\mathrm{e}^{\omega\theta}\cos\frac{\theta}{2}\sin\theta \Bigg\}
\end{aligned}
\tag{20}
$$

It is worth noting that functions (20) cannot be used for orthotropic bimaterial problems, because the oscillatory index ω is computed from isotropic material properties, which are not known for orthotropic bimaterials.

It is also important to note that the enrichment functions (18) correspond only to Type I of each composite layer, as defined by the complex roots of the characteristic equation (5). This is similar to the unidirectional orthotropic enrichment functions previously proposed by Asadpoure *et al.* [39]:

$$
\{F_l(r,\theta)\}_{l=1}^4 = \left\{ \sqrt{r}\cos\frac{\theta_1}{2}\sqrt{g_1(\theta)}, \sqrt{r}\cos\frac{\theta_2}{2}\sqrt{g_2(\theta)}, \sqrt{r}\sin\frac{\theta_1}{2}\sqrt{g_1(\theta)}, \sqrt{r}\sin\frac{\theta_2}{2}\sqrt{g_2(\theta)} \right\} \tag{21}
$$

$$
g_i(\theta) = \left(\cos^2\theta + \frac{\sin^2\theta}{p_j^2} \right)^{1/2}, \quad j = 1,2 \tag{22}
$$

$$
\theta_j = tg^{-1}\left(\frac{y}{p_j x} \right) = tg^{-1}\left(\frac{tg\theta}{p_j} \right) \tag{23}
$$

3.2.3. Modeling weak discontinuities. In the presence of weak discontinuity in an arbitrary finite element, the enrichment part of the XFEM approximation ($\boldsymbol{u}_{\text{weak}}^{\text{enr}}$) can be defined by replacing the heaviside function $H(\boldsymbol{x})$ with an appropriate enrichment function $\chi(\boldsymbol{x})$ [62]:

$$
\boldsymbol{u}_{\text{weak}}^{\text{enr}}(\boldsymbol{x}) = \sum_{\substack{r \\ n_r = N^\chi}} c_r \phi_r(\boldsymbol{x}) \chi_r(\boldsymbol{x}) \tag{24}
$$

where $\chi(\boldsymbol{x})$ is the weak discontinuous enrichment function defined in terms of the signed distance function as:

$$
\chi_r(\boldsymbol{x}) = |\xi(\boldsymbol{x})| \tag{25}
$$

$$
\xi(\boldsymbol{x}) = \min \|\boldsymbol{x} - \boldsymbol{x}_\Gamma\| \operatorname{sign}[e_n(\boldsymbol{x} - \boldsymbol{x}_\Gamma)] \tag{26}
$$

where $\boldsymbol{x}$, $\boldsymbol{x}_\Gamma (\boldsymbol{x}_\Gamma \in \Gamma)$, and $\boldsymbol{e_n}$ are defined in Figure 3.

DOI: 10.1002/nme

This enrichment is used where the displacement fields remain continuous whereas the strain fields are discontinuous.

It should be noted that the weak discontinuity enrichment function is used only for the elements that are cut by the interface, avoiding generation of excessive errors in surrounding elements. Alternative functions are also available; e.g. Moës *et al.* [63] has proposed a ridge enrichment function that is centered on the interface and has zero value on the elements not crossed by the interface.

4. DISCRETIZATION AND INTEGRATION

The discrete system of linear equations using the XFEM procedure in global form can be written as:

$$\boldsymbol{K}\boldsymbol{d}=\boldsymbol{f} \tag{27}$$

where $\boldsymbol{d}$ is the vector of nodal degrees of freedom for both classical and enriched ones, as defined in Equation (28):

$$\boldsymbol{d}=\{\boldsymbol{u}\ \ \boldsymbol{a}\ \ \boldsymbol{b}\ \ \boldsymbol{c}\} \tag{28}$$

$\boldsymbol{K}$ is the stiffness matrix and $\boldsymbol{f}$ is the vector of external force. The global stiffness matrix and force vector are calculated by assembling element stiffness matrix and force vector. f_i for each element e is assembled from the following standard and enrichment components:

$$\boldsymbol{f}_i^u=\int_{\Gamma_t^e}\phi_i\bar{\boldsymbol{t}}\,\mathrm{d}\Gamma+\int_{\Omega^e}\phi_i\boldsymbol{b}\,\mathrm{d}\Omega \tag{29}$$

$$f_i^a=\int_{\Gamma_t^e}\phi_i H\bar{\mathbf{t}}\,\mathrm{d}\Gamma+\int_{\Omega^e}\phi_i H\mathbf{b}\,\mathrm{d}\Omega \tag{30}$$

$$f_i^b=\int_{\Gamma_t^e}\phi_i F_\alpha\bar{\mathbf{t}}\,\mathrm{d}\Gamma+\int_{\Omega^e}\phi_i F_\alpha\mathbf{b}\,\mathrm{d}\Omega\quad(\alpha=1,\ldots,8) \tag{31}$$

$$f_i^c=\int_{\Gamma_t^e}\phi_i\chi\bar{\mathbf{t}}\,\mathrm{d}\Gamma+\int_{\Omega^e}\phi_i\chi\mathbf{b}\,\mathrm{d}\Omega \tag{32}$$

where Ω^e is the volume or surface of element e and Γ_t^e is the traction boundary of element e, $\bar{\boldsymbol{t}}$ is the traction, and $\boldsymbol{b}$ is the body force. Evaluation of (32) becomes important when a χ-enriched element (weak discontinuity or material interface) is subjected to a traction boundary condition.

Similarly, $\boldsymbol{k}_{ij}$ for the element e is assembled from the following standard and enrichment components:

$$\boldsymbol{k}_{ij}^{rs}=\int_{\Omega^e}(\boldsymbol{B}_i^r)^{\mathrm{T}}\boldsymbol{D}\boldsymbol{B}_j^s\,\mathrm{d}\Omega\quad(r,s=u,a,b,c) \tag{33}$$

$$\boldsymbol{k}_{ij}^{ac}=\boldsymbol{k}_{ij}^{ca}=0 \tag{34}$$

$\boldsymbol{B}$ is the matrix of shape function derivatives defined as [29]:

$$\boldsymbol{B}_i^u=\begin{bmatrix}\phi_{i,x} & 0\\ 0 & \phi_{i,y}\\ \phi_{i,y} & \phi_{i,x}\end{bmatrix} \tag{35}$$

DOI: 10.1002/nme

$$\boldsymbol{B}_i^a = \begin{bmatrix} (\phi_i[H(\xi)-H(\xi_i)])_{,x} & 0 \\ 0 & (\phi_i[H(\xi)-H(\xi_i)])_{,y} \\ (\phi_i[H(\xi)-H(\xi_i)])_{,y} & (\phi_i[H(\xi)-H(\xi_i)])_{,x} \end{bmatrix} \tag{36}$$

$$\boldsymbol{B}_i^{b\alpha} = \begin{bmatrix} (\phi_i[F_\alpha - F_{\alpha_i}])_{,x} & 0 \\ 0 & (\phi_i[F_\alpha - F_{\alpha_i}])_{,y} \\ (\phi_i[F_\alpha - F_{\alpha_i}])_{,y} & (\phi_i[F_\alpha - F_{\alpha_i}])_{,x} \end{bmatrix} \quad (\alpha = 1, \ldots, 8) \tag{37}$$

$$\boldsymbol{B}_i^c = \begin{bmatrix} (\phi_i \chi)_{,x} & 0 \\ 0 & (\phi_i \chi)_{,y} \\ (\phi_i \chi)_{,y} & (\phi_i \chi)_{,x} \end{bmatrix} \tag{38}$$

In elements cut by a crack or an interface, the ordinary Gaussian rules do not accurately calculate the integration over the enriched elements. In order to overcome this numerical integration problem, these elements are subdivided at both sides of the crack or interface into sub-triangles whose edges are adapted to crack faces or the interface, as illustrated in Figure 4. In this partitioning method, if values of $S^-/(S^+ + S^-)$ or $S^+/(S^+ + S^-)$, where S^+ and S^- are the area of the influence domain of a node above and below the crack, respectively (see Figure 5), are smaller than an allowable tolerance value, the node must not be enriched to avoid numerical problems. The tolerance value proposed by Dolbow *et al.* [33] is 0.01%.

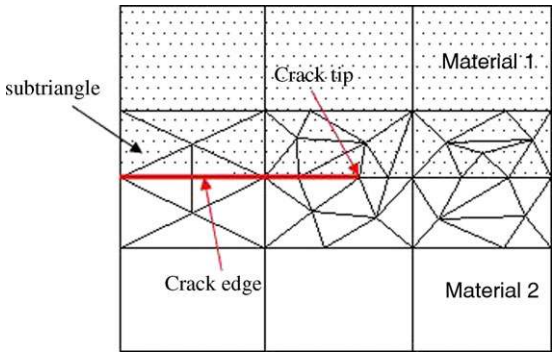

Figure 4. Cracked and bimaterial elements are subdivided into sub-triangles.

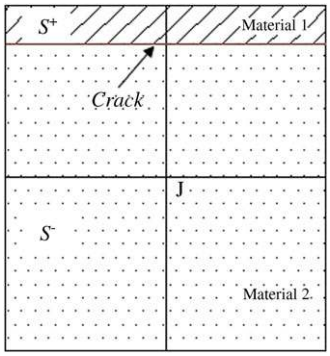

Figure 5. S^+ and S^- for the node J in its influence domain (shaded area).

DOI: 10.1002/nme

5. EVALUATION OF SIFS

In this study, the domain integral method, developed by Chow *et al.* [64], is utilized to evaluate mixed-mode SIFs for an interfacial crack between two orthotropic materials [65]:

$$J = \int_A (\sigma_{ij} u_{i,1} - W\delta_{1j}) q_{,j} \, \mathrm{d}A \tag{39}$$

where W is the strain energy density, defined by $W = (1/2)\sigma_{ij}\varepsilon_{ij}$ for linear-elastic materials, A is the area surrounding the crack-tip; the interior region of Γ (Figure 6), and q is a function smoothly varying from $q = 1$ at crack-tip to $q = 0$ at exterior boundary, Γ.

In the interaction integral method, auxiliary fields are introduced and superimposed onto the actual fields to satisfy the boundary value problem (equilibrium equation and traction-free boundary condition on crack surfaces) to extract the mixed-mode SIFs [66]. One of the choices for the auxiliary state is the displacement and stress fields in the vicinity of the interfacial crack-tip (Appendix A).

The J^S integral for the sum of the two states can be defined as:

$$J^S = J + J^{\mathrm{aux}} + M \tag{40}$$

where J and J^{aux} are associated with the actual and auxiliary states, respectively, and M is the interaction integral, defined as

$$M = \int_A [\sigma_{ij} u_{i,1}^{\mathrm{aux}} + \sigma_{ij}^{\mathrm{aux}} u_{i,1} - W^{(1,2)}\delta_{1j}] q_{,j} \, \mathrm{d}A \tag{41}$$

For linear-elastic condition, $W^{(1,2)}$ is defined as:

$$W^{(1,2)} = \tfrac{1}{2}(\sigma_{ij}\varepsilon_{ij}^{\mathrm{aux}} + \sigma_{ij}^{\mathrm{aux}}\varepsilon_{ij}) \tag{42}$$

where superscript aux stands for the auxiliary state. The M integral shares the same path-independent property of J integral. As a result, it can be calculated away from the crack-tip where the finite element solution is more accurate.

In order to determine the SIFs of the present orthotropic bimaterial problem from the M integral, the method proposed by Chow *et al.* [64] is adopted. Consider two independent equilibrium states of an elastically deformed bimaterial body (actual and auxiliary states) with the two independent displacement fields being denoted by u and u^{aux}. The SIFs are related to M by [64]

$$k_i = 2 \sum_{m=1}^{2} U_{im} M\{u, u^{aux(m)}\} \quad (i = 1, 2) \tag{43}$$

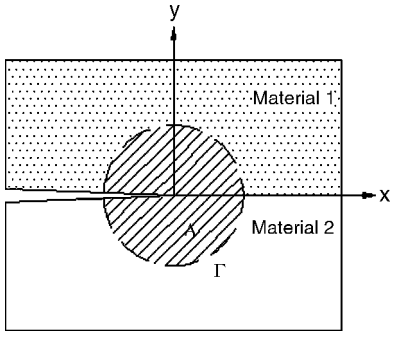

Figure 6. The contour Γ and its interior area, A [58].

DOI: 10.1002/nme

where $u^{\text{aux}(1)}$ and $u^{\text{aux}(2)}$ are the auxiliary states with $K_1=1$, $K_2=0$ and $K_1=0$, $K_2=1$, respectively, and

$$U=[[(L_{\#1}^{-1}+L_{\#2}^{-1})]^{-1}(I+\hat{\beta}^2)]^{-1} \tag{44}$$

$$\hat{\beta}=(L_{\#1}^{-1}+L_{\#2}^{-1})(S_{\#1}L_{\#1}^{-1}-S_{\#2}L_{\#2}^{-1}) \tag{45}$$

The subscripts #1 and #2 denote the upper and lower materials and S and L are 2×2 real Barnett and Lothe tensors, respectively [67]. Explicit expressions of non-zero components of S and L for an orthotropic material have been derived by Dongye and Ting [68] and Deng [69],

$$S_{21}=\left[\frac{C_{66}\left(\sqrt{C_{11}C_{22}}-C_{12}\right)}{C_{22}\left(C_{12}+2C_{66}+\sqrt{C_{11}C_{22}}\right)}\right]^{1/2},\quad S_{12}=-\sqrt{\frac{C_{22}}{C_{11}}}S_{21} \tag{46}$$

$$L_{11}=\left(C_{12}+\sqrt{C_{11}C_{22}}\right)S_{21},\quad L_{22}=\sqrt{\frac{C_{22}}{C_{11}}}L_{11} \tag{47}$$

where C_{ij} is the contracted form of the fourth-order elastic constant tensor $C_{ijkl}=S_{ijk}^{-1}$. Components of S and L are computed for each individual layer.

6. NUMERICAL EXAMPLES

6.1. Tensile orthotropic plate with a central crack

In this example, a crack in an orthotropic medium is simulated by the use of proposed orthotropic bimaterial enrichment functions. This is in fact a test to verify the proposed approach for modeling two similar orthotropic layers and to compare the results with available data for a single orthotropic layer. The crack is aligned along one of the axes of orthotropy in the center of the plate. Figure 7 illustrates the geometry and boundary conditions of the cracked plate. At edges parallel to the crack, a constant tensile traction is applied by utilizing a uniform unit traction ($\sigma=1$) and the analysis is performed in the plane stress state. The plate is composed of a graphite-epoxy material with the following orthotropic properties:

$$E_1=114.8\,\text{GPa},\quad E_2=11.7\,\text{GPa},\quad G_{12}=9.66\,\text{GPa},\quad v_{12}=0.21$$

In order to create the finite element model of the problem, the domain was discretized uniformly into 2025 four-noded quadrilateral elements (2116 nodes); 45 rows of elements in x_1 and x_2 directions each.

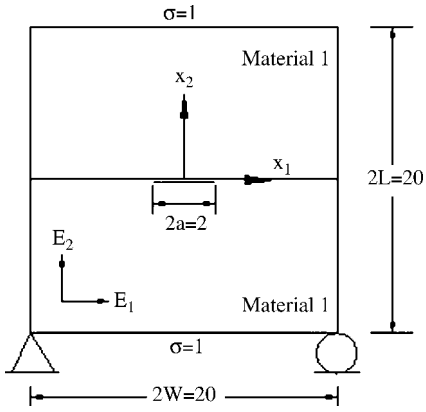

Figure 7. The geometry and boundary conditions for a plate with a crack parallel to material axes of orthotropy.

DOI: 10.1002/nme

Table I. Values of SIFs for a plate with a crack parallel to material axes of orthotropy.

Method	K_{I}	K_{II}	Number of elements	DOF
Kim and Paulino [70]	1.767	0	2001	11 702
Asadpoure *et al.* [39]	1.804	0	2025	4278
Asadpoure and Mohammadi [41]	1.807	0	2025	4278
Present method	1.777	0	2025	4278

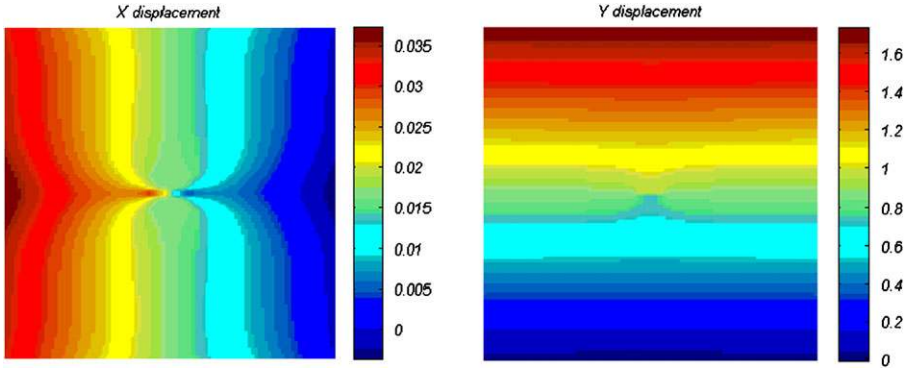

Figure 8. X and Y displacement contours.

The new orthotropic enrichment functions for a bimaterial interface crack are used for simulating the crack-tip singular stress state, while the material properties of the two sides of the crack are assumed to be the same. As a result, no weak discontinuity enrichment function is required in the model.

SIFs are calculated by the J integral method presented in Section 5. The SIFs are compared with the results reported by Kim and Paulino [70] and Asadpoure *et al.* [39] and Asadpoure and Mohammadi [41] in Table I. Kim and Paulino [70] used a total of 2001 elements and 5851 nodes while Asadpoure *et al.* [39] and Asadpoure and Mohammadi [41] utilized the XFEM with different orthotropic enrichment functions for a crack in an orthotropic medium, using an adaptive mesh, refined around the crack, with 2025 four-noded quadrilateral elements and 2116 nodes.

The SIF of the present method in mode I is different about 0.6% from Kim and Paulino's report [70]; however, they used almost three times the present degrees of freedom. Also, it is observed that the mode I SIF is only different about 1.5% from Asadpoure *et al.* [39] and 1.7% from Asadpour and Mohammadi [41]; although a uniform mesh was adopted in the present model.

The displacement and stress contours are illustrated in Figures 8 and 9.

6.2. *Central crack in an infinite bimaterial plate*

This example is dedicated to the analysis of a crack in a bimaterial plate, previously studied by Chow *et al.* [64]. An interfacial crack at the center of a bimaterial block is considered. The block consisted of two different materials with the plane strain condition. The dimensions of the rectangular plate and the crack are:

$$a = 1\,\mathrm{m}, \quad W = 20a, \quad h = 20a$$

A remote unit tensile loading, $\sigma^0_{22} = 1\,\mathrm{Mpa}$, is applied to the block, as illustrated in Figure 10. Qian and Sun [25] have demonstrated that in order to use a finite bimaterial model as a representation of the infinite bimaterial plate, the following condition must be held in terms of the boundary tractions σ^1_{11} and σ^2_{11} (Figure 10) and the components of the compliance tensor S_{ijkl}:

$$S^1_{1111}\sigma^1_{11} - S^2_{1111}\sigma^2_{11} = (S^2_{11122} - S^1_{1122})\sigma^0_{22} \tag{48}$$

DOI: 10.1002/nme

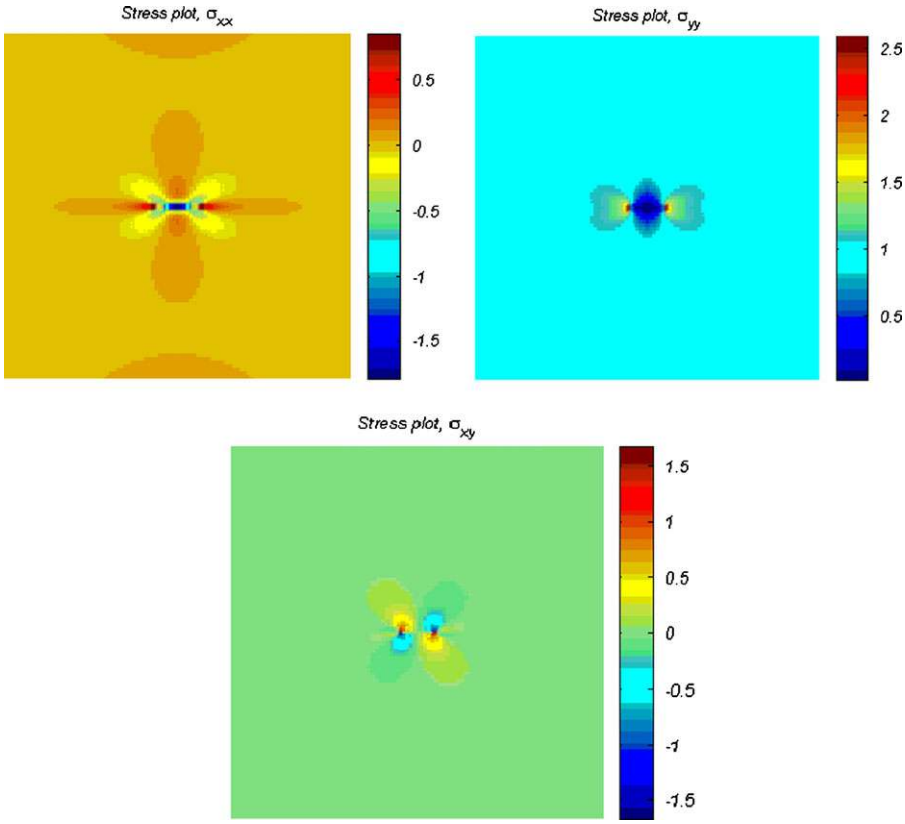

Figure 9. σ_{xx}, σ_{yy}, and σ_{xy} stress contours.

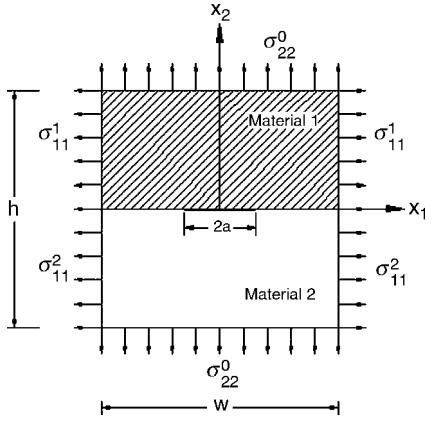

Figure 10. The geometry and boundary conditions of a bimaterial interface crack [64].

The following boundary tractions that satisfy Equation (48) can then be derived as: [64]

$$\sigma_{11}^{1} = 0 \tag{49}$$

$$\sigma_{11}^{2} = \left[\frac{v_{12_{\#2}} + v_{13_{\#2}} v_{32_{\#2}}}{1 - v_{13_{\#2}} v_{31_{\#2}}} - \frac{v_{12_{\#2}} + v_{13_{\#2}} v_{32_{\#2}}}{1 - v_{13_{\#2}} v_{31_{\#2}}} \left(\frac{E_{1_{\#2}}}{E_{1_{\#1}}} \right) \right] \sigma_{22}^{\circ} \tag{50}$$

DOI: 10.1002/nme

Both layers are orthotropic materials and the fiber directions are along the x_3 axis (out of plane direction) in material 1 and along the x_1 axis in material 2 with the following properties [64]:
Material 1

$$E_3 = 142\,\text{Gpa}, \quad \frac{E_1}{E_3} = \frac{E_2}{E_3} = 6.91 \times 10^{-2}$$

$$\frac{G_{12}}{E_3} = 2.68 \times 10^{-2}, \quad \frac{G_{13}}{E_3} = \frac{G_{23}}{E_3} = 4.23 \times 10^{-2}$$

$$v_{31} = v_{32} = v_{12} = 0.3$$

Material 2

$$E_1 = 142\,\text{Gpa}, \quad \frac{E_2}{E_1} = \frac{E_3}{E_1} = 6.91 \times 10^{-2}$$

$$\frac{G_{23}}{E_1} = 2.68 \times 10^{-2}, \quad \frac{G_{13}}{E_1} = \frac{G_{12}}{E_1} = 4.23 \times 10^{-2}$$

$$v_{12} = v_{13} = v_{23} = 0.3$$

The analytical SIFs for a crack between two anisotropic materials in the plate, which were derived by Qu and Bassani [71], can be expressed as:

$$k^{\infty} = \sqrt{\pi a}\boldsymbol{Y}[(1+2i\varepsilon)(2\text{a})^{-i\varepsilon}]\boldsymbol{t}^0 \tag{51}$$

where

$$k^{\infty} = \{K_2^{\infty}, K_1^{\infty}, K_3^{\infty}\} \tag{52}$$

$$\boldsymbol{t}^0 = \{\sigma_{12}^0, \sigma_{22}^0, \sigma_{23}^0\}^{\mathrm{T}} \tag{53}$$

For the present problem $\sigma_{12}^{\circ} = \sigma_{23}^{\circ} = 0$; hence, the analytical SIFs are calculated as:

$$K_1^{\infty} = 1.778, \quad K_2^{\infty} = 0.146$$

Owing to symmetry along the x_2 axis, only one half of the problem is modeled. A model similar to Figure 11 with 241 four-noded quadrilateral elements and 260 nodes is used to simulate the problem and the element that contains a crack-tip is modeled with the new orthotropic enrichment functions.

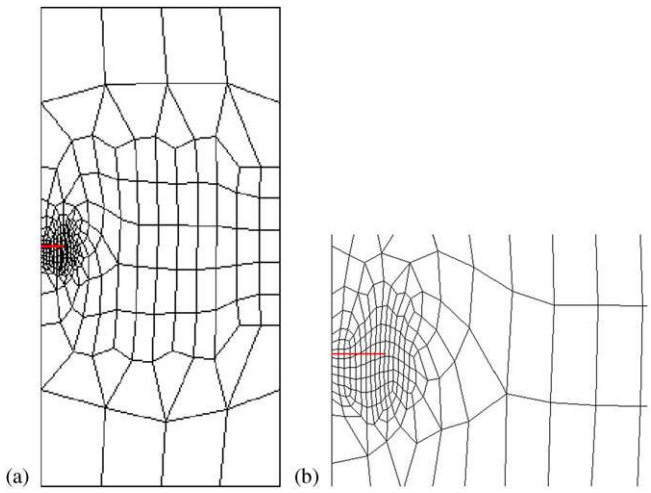

Figure 11. FEM discretization for a single edge crack in a bimaterial rectangular plate: (a) whole view of FEM mesh and (b) details of descretization around the crack-tip.

DOI: 10.1002/nme

In this example, a 2×2 Gauss quadrature rule is applied to evaluate the stiffness matrix of regular finite elements, whereas the quadrature partitioning approach (Section 4) is used for integration over enriched elements. Any element enriched with heaviside or weak discontinuity functions is numerically partitioned into four sub-triangles to accurately calculate the numerical integrals. Elements enriched with tip-enrichments have far more complex shape functions than classical finite element shape functions. As a result, they are partitioned into six sub-triangles and seven gauss points are utilized for integrations in each sub-triangle. The initial value of the relative integration domain size, r_d (radius of the J integral domain), is assumed to be one-third of crack length in the present XFEM analysis.

Evaluation of Equation (32) is important in this case, because the element placed on the material interface (a weak discontinuity) and next to the right edge of the plate should correctly evaluate Equation (32) in order to take into account the interactive contribution of traction and enriched degrees of freedom. (Note that in this particular case, the computed value of traction $\sigma_{11}^2 = 4.02\,\text{Mpa}$ is about four times the value of applied tensile loading $\sigma_{22}^{\circ} = 1\,\text{Mpa}$).

Table II compares the differences between the exact solution by Qu and Bassani [71] with the mixed-mode SIFs obtained by XFEM and the results reported by Chow *et al.* [64]. In Chow *et al.* [64], the SIFs are calculated using a hybrid element method and the mutual integral. In their models, conforming eight-noded isoparametric elements are the primary elements used to mesh the bimaterial block and the interfacial crack-tip is modeled either with hybrid elements or with standard quarter-point elements for both the mutual integral method and the extrapolation technique.

The results show that with more or less similar number of nodes, XFEM more accurately evaluates both SIFs. The method of hybrid elements may have used slightly less number of nodes, but its accuracy in evaluation of mode I SIF is almost one-tenth of XFEM. In addition, the present XFEM method is capable of solving variable length cracks and propagation problems on a fixed mesh, which is a major advantage on other available techniques such as hybrid elements.

In order to assess the level of accuracy provided by the new enrichment functions, XFEM analyses are now performed in three cases; with and without the new crack-tip enrichment functions, and with the original isotropic crack-tip functions in a single material. Heaviside enrichments are adopted in all three cases. Table III compares the computed SIFs and the relative errors for these three cases. Clearly, inclusion of the new enrichments has substantially improved the results.

Table II. Values of SIFs relative errors (%) for a bimaterial plate with an edge crack.

Method		Number of elements	Number of nodes	Error (K_{I})	Error (K_{II})
Chow *et al.* [64]	Hybrid element	56	205	0.79	1.37
	Mutual integral	216	679	0.67	0.68
	Mutual integral	72	237	0.56	7.53
	Extrapolation	72	237	7.09	21.92
	Extrapolation	216	679	8.27	10.27
Present method	XFEM	241	260	0.011	1.164

Table III. Comparison of SIFs with and without crack-tip enrichment functions.

	$H(x)+F(x)$	Only $H(x)^*$	$H(x)+F'(x)^{\dagger}$	$H(x)+F'(x)^{\ddagger}$
K_{I}	1.7778	1.5758	1.5516	0.6423
K_{II}	0.1477	0.1631	0.1877	0.1021
Error (K_{I})	0.011	11.372	12.73	63.87
Error (K_{II})	1.164	11.712	28.56	169.93

*To avoid extensive error, the mesh is locally adapted to place the crack-tip near the element edge.
†Isotropic enrichments with orthotropic auxiliary fields.
‡Isotropic enrichments with isotropic auxiliary fields based on average material properties.

DOI: 10.1002/nme

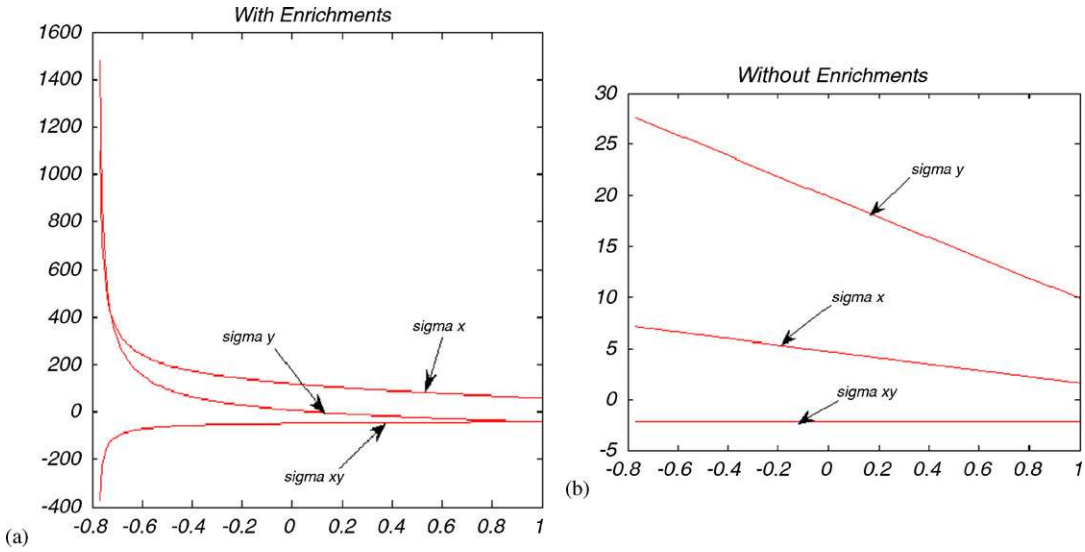

Figure 12. Comparison of stress fields around the crack-tip: (a) with crack-tip enrichments and (b) without crack-tip enrichments. The crack-tip is located at $(-0.8, 0)$ in the local curvilinear coordinates of the tip element.

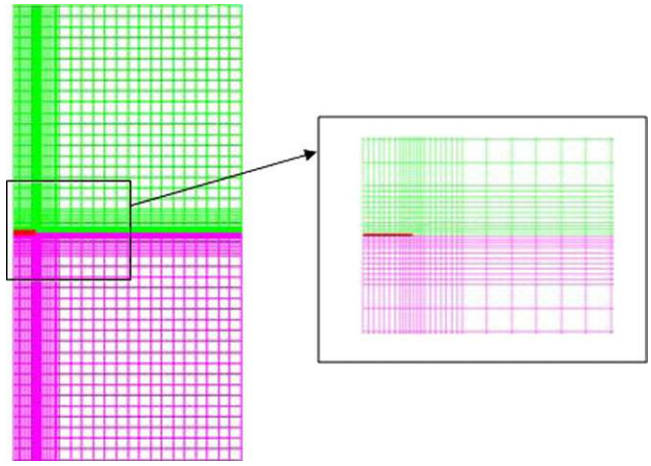

Figure 13. Adaptively structured finite element mesh for investigating the effect of relative J integral domain size.

Additionally, the effect of new tip-enrichments is investigated by comparing the variations of stress components on the crack-tip element, as depicted in Figure 12. Clearly, inclusion of new enrichments has resembled the singular nature of stress field near the crack-tip, whereas, without the tip-enrichments, far lower levels of finite values of stress components are obtained.

The effect of different sizes of the relative J integral domain (r_d) on the values of SIFs is illustrated in Figure 14 based on the adaptively structured mesh, shown in Figure 13. The results are calculated for the range of relative J integral domain size (r_d) of about 0.04–0.25 of crack length, which correspond to 2–10 elements far from the crack-tip, respectively. According to Figures 17 and 18, as the domain size r_d reaches to about $0.15a$, the results become domain independent.

Also, a number of unstructured and structured mesh models (Figures 13 and 15) are used with different sizes of elements in order to assess the effect of mesh refinement around the crack. According to Table IV, refining the mesh around the crack has significantly more effect in reducing the error of evaluation of mode II SIF than evaluation of K_1. Nevertheless, the overall error remains well within the acceptable range, indicating the mesh independency of the results.

DOI: 10.1002/nme

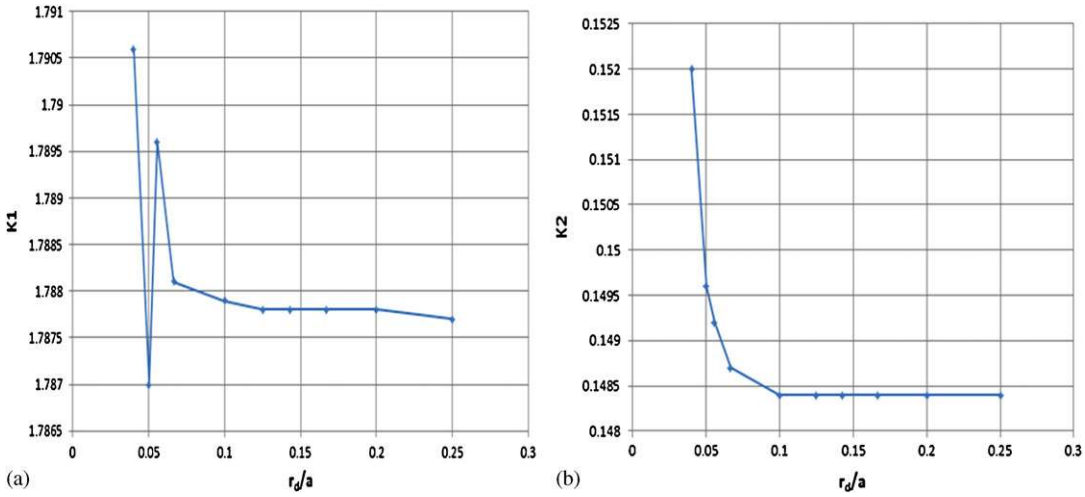

Figure 14. Variations of the mode I and II stress intensity factors with respect to r_d/a: (a) mode I and (b) mode II.

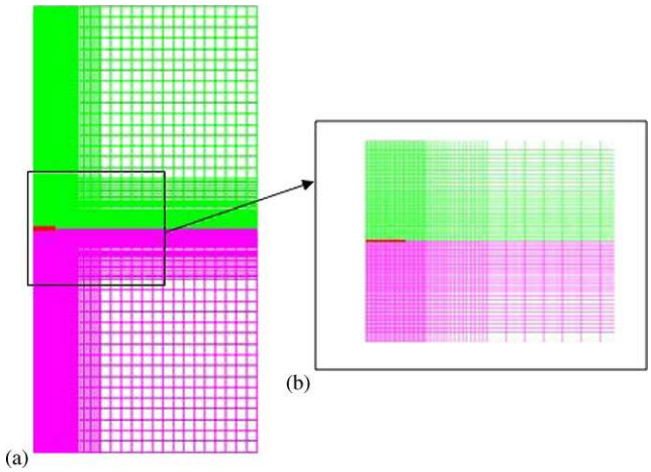

Figure 15. FEM discretization when the mesh is refined around the crack: (a) whole view of FEM discretization model and (b) discretization around the crack-tip.

Table IV. Mixed-mode stress intensity factors for different meshes.

Number of elements along the crack length	Mesh type	$\frac{r_d}{a}$	K_{I}	K_{II}	Error (K_{I}) (%)	Error (K_{II}) (%)
20	Structured	0.33	1.7920	0.1477	0.787	1.164
36	Structured	0.33	1.79	0.1467	0.675	0.479
47	Structured	0.33	1.79	0.1466	0.675	0.411
57	Structured	0.2	1.79	0.1465	0.675	0.342
9	Unstructured	0.2	1.7595	0.1464	−1.040	0.274
14	Unstructured	0.2	1.7646	0.147	−0.754	0.685
12	Unstructured	0.3333	1.7778	0.1477	−0.011	1.164

Finally, a crack propagation problem is idealized in this problem to illustrate the efficiency of the present XFEM for simulation of several crack lengths on a fixed finite element mesh. Here, the interlaminar crack is bound to extend only along the material interface. As a result, no particular

DOI: 10.1002/nme

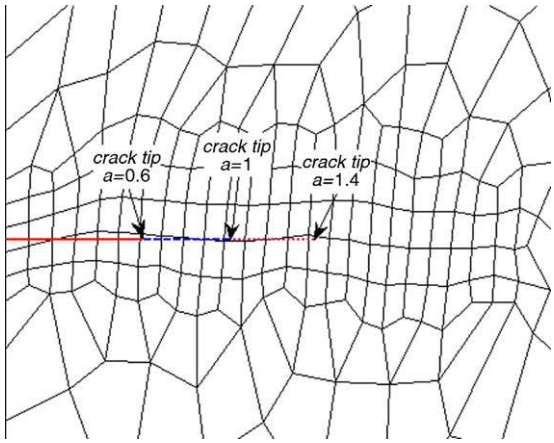

Figure 16. A fixed unstructured finite element mesh for investigating the crack propagation process by analyzing three different crack lengths.

Table V. Mixed-mode stress intensity factors for different crack lengths on a fixed mesh of 514 elements and 540 nodes.

	Exact (Equation (51))			XFEM		Error %	
Crack length	K_{I}	K_{II}	r_d	K_{I}	K_{II}	K_{I}	K_{II}
0.6	1.3743	0.1574	0.33	1.3757	0.1554	0.102	1.271
1	1.7781	0.146	a/3	1.7755	0.1475	0.146	1.027
1.4	2.1062	0.128	a/3	2.1251	0.1293	0.897	1.016

propagation criterion is necessary in examining this characteristic of present XFEM, and instead, only three different crack lengths: 0.6, 1.0, and 1.4 are assumed to be generated through the propagation process and they are analyzed with a fixed finite element mesh, partially shown in Figure 16. According to Table V, very good quality results are obtained for all three cases.

6.3. Central crack in an infinite bimaterial orthotropic plate

In this example, the stability of a crack in the interface of two orthotropic materials, as depicted in Figure 17, is studied. The infinite plate is subjected to a remote unit tensile loading σ_{22}^0, with the plane strain condition. The material properties of the T300-5208 graphite epoxy are defined as:

$$E_T = E_Z = 10.8\,\mathrm{GPa}, \quad E_L = 137\,\mathrm{GPa}$$

$$G_{ZL} = G_{TL} = 5.65\,\mathrm{GPa}, \quad G_{ZT} = 3.36\,\mathrm{GPa}$$

$$v_{ZL} = v_{TL} = 0.238, \quad v_{TZ} = 3.36$$

where L, T, Z are longitudinal, transverse, and through the thickness directions, respectively. The present example is for a $[90^\circ/0^\circ]$ bimaterial block. The fiber direction in the 90° lamina is along the x_1 axis whereas for the 0° lamina, the fiber direction lies along the x_3 axis (out of plane direction). The dimensions of the plate are:

$$\frac{W}{a} = \frac{h}{a}, \quad a = 1\,\mathrm{m}$$

Only one-half of the problem is modeled due to symmetry along the x_2 axis. A finite element model with 250 elements and 268 nodes is employed (Figure 18(a)) and the crack-tip is modeled with new orthotropic enrichment functions. A Gauss quadrature rule, similar to the previous

DOI: 10.1002/nme

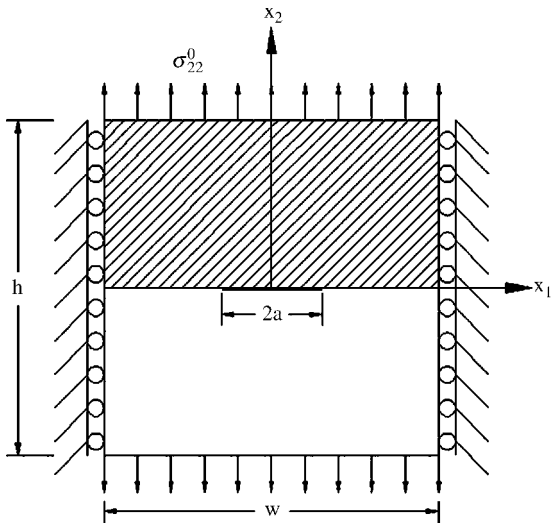

Figure 17. An interfacial crack between two orthotropic materials.

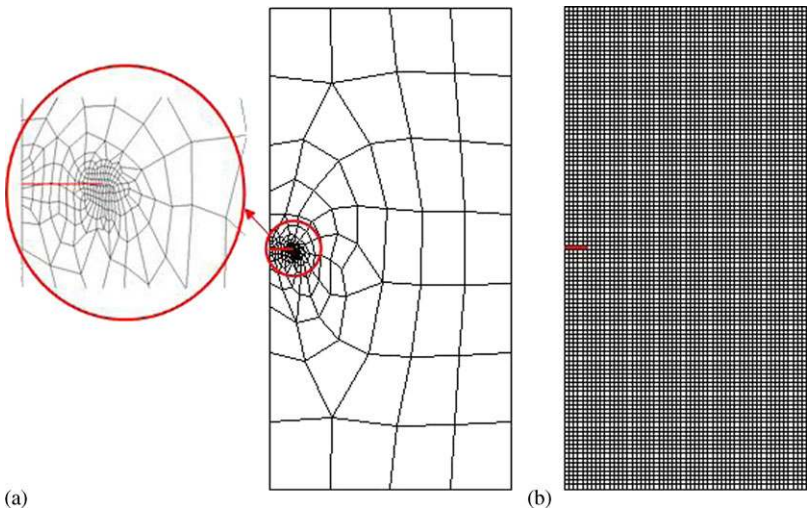

Figure 18. FEM discretizations: (a) unstructured FEM model (type 1) and (b) uniform FEM discretization (type 2).

example, is used and the relative J integral domain size, r_d, is set to one-third of the crack length.

To determine the accuracy of the approach, comparisons are made with the exact solution of an infinite anisotropic bimaterial block provided by Qu and Bassani [71], and another investigation by Chow and Atluri [72], based on the standard eight-noded quarter-point elements and using both the mutual integral method and the extrapolation technique.

Table VI depicts the results of SIFs obtained by different methods and the extent of error with respect to the analytical solution. Clearly, very accurate results are obtained by the new XFEM formulation.

It is also observed that using more gauss points in the tip element does not necessarily lead to more accurate results. The reason may be attributed to the fact that the Gauss quadrature rule is basically designed to accurately determine the position and weighting factors for integration of polynomial integrands, and for non-polynomial integrands (as in the present case) there is an optimal value for the number of Gauss points, beyond that the accuracy may even decrease.

DOI: 10.1002/nme

Table VI. Stress intensity factors obtained by different methods compared with the analytical solution by Qu and Bassani [71].

Method		Number of elements	Number of nodes	Error (K_{I})	Error (K_{II})
Chow and Atluri [72]	Mutual integral	216	679	0.6	0.1
	Mutual integral	72	237	0.7	13.6
	Extrapolation	72	237	9.5	6.9
	Extrapolation	216	679	13.1	2.3
Present method	XFEM with 78 Gauss points in tip element	250	268	0.051	0.824
	XFEM with 42 Gauss points in tip element	250	268	0.068	0.353

Table VII. Comparison of stress intensity factors with/without crack-tip enrichment functions.

	$H(x)+F(x)$	Only $H(x)$
K_{I}	1.7757	1.778
K_{II}	0.0847	0.0749
Error (K_{I})	0.068	0.197
Error (K_{II})	0.353	11.882

Table VIII. Comparison of stress intensity factors with different number of Gauss points in the crack-tip element.

	Number of Gauss points			
	6	18	42	78
K_{I}	1.7779	1.7769	1.7757	1.7754
K_{II}	0.088	0.0838	0.0847	0.0843
Error (K_{I})	0.192	0.135	0.068	0.051
Error (K_{II})	3.529	1.412	0.353	0.824

Similarly, Sukumar *et al.* [32] have demonstrated that a simple increase in the order and number of Gauss points for a Heaviside-enriched element does not provide accurate solution. This is also observed in many meshless-based weak-form solutions.

The effect of employing the crack-tip enrichment function is illustrated in Table VII. The results are compared with the special case where only the heaviside function is used along the whole crack length, while the crack-tip is located just off the edge of tip element.

It is clearly seen that the effect of crack-tip enrichments are higher for evaluation of K_{II}. Also, different values may be obtained for different meshes and J integral domain sizes. Far lower level of accuracies are expected for the H-only analysis if the crack-tip is positioned well inside the tip element.

The effect of using different number of gauss points in the crack-tip element is illustrated in Table VIII. The quadrature partitioning approach (Section 4) is used for integration in tip element and the tip element is partitioned into six sub-triangles. The value of the relative integration domain size, r_d, is assumed to be one-third of crack length.

The effect of larger tip-enrichment zone is illustrated in Table IX. Figure 19 shows two different enrichment zones. Squares are the nodes that are enriched by tip-enrichment functions (larger zone), while * indicates the smaller zone (just one tip element).

It is observed that the larger tip-enrichment zone does not result in better evaluation of SIFs in this example. The reason for this small increased inaccuracy may be attributed to the fact that

DOI: 10.1002/nme

Table IX. Stress intensity factors with different tip-enrichment zones.

	One enriched tip element (One layer of tip enrichment)	Nine enriched tip elements (Two layers of tip enrichment)
K_{I}	1.7757	1.7765
K_{II}	0.0847	0.0859
Error (K_{I})	0.068	0.113
Error (K_{II})	0.353	1.059

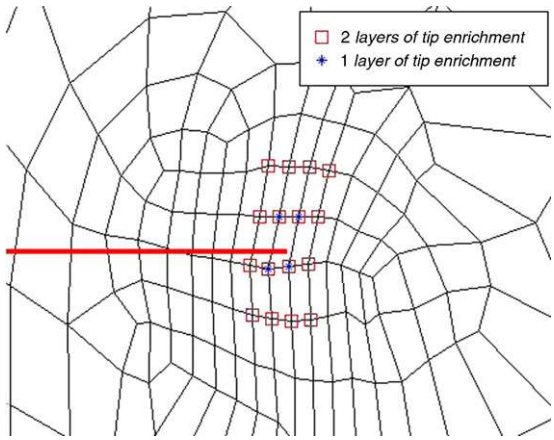

Figure 19. Different tip-enrichment zones.

the analytical stress and displacement solutions are based on the simplifications that are only valid in the vicinity of crack-tip. As a result, a reduction in accuracy may be observed if a large area around the crack-tip is enriched. For the present case, this reduction is very small and negligible and may vary for different sizes of crack-tip elements.

The effect of mesh refinement around the crack is also investigated by utilizing three types of structured and unstructured (Figures 15 and 18) meshes with different sizes of elements (indicated by the number of elements along the crack length). Table X compares the results of XFEM simulations using the different types of discretization and relative J integral domain sizes (r_d). It can be concluded that accurate evaluation of mode II SIF is more sensitive and requires a refined mesh around the crack with a relative J integral domain size of about $0.2a$. Again, evaluation of K_{I} remains less sensitive to these variations.

Displacement and stress contours of the present example are plotted in Figures 20 and 21. The results are based on an adaptively structured mesh with 28 elements along the crack length.

6.4. Isotropic–orthotropic bimaterial crack

In this example, an interface crack between isotropic and orthotropic layers of a tensile bimaterial specimen is investigated. The analysis is performed for the bimaterial plate in a plane stress state, subjected to a remote tensile loading and for a range of crack lengths. Figure 22 shows the geometry and the nominal dimensions of the problem.

The layer above the interface is an isotropic PSM-1 material and the material below the interface is composed of orthotropic Scotch ply 1002 (a unidirectional glass fiber-reinforced composite in epoxy matrix). Table XI defines the necessary material properties.

In Table XI, L is the direction of fibers and T denotes the direction transverse to fibers. Two fiber orientations are considered for material 2, fibers parallel to the interface ($\alpha = 0^\circ$) and fibers perpendicular to the interface ($\alpha = 90^\circ$).

DOI: 10.1002/nme

Table X. Mixed-mode stress intensity factors using a refined mesh within the crack length.

Mesh type	Number of elements along the crack length	$\frac{r_d}{a}$	K_{I}	K_{II}	Error (K_{I}) (%)	Error (K_{II}) (%)
Uniformly structured	6	0.369	1.7835	0.0976	0.507	14.824
	8	0.262	1.7864	0.093	0.671	9.412
	10	0.229	1.7858	0.0905	0.637	6.471
	12	0.2	1.7861	0.0896	0.654	5.412
	13	0.2	1.786	0.0883	0.648	3.882
	15	0.2	1.788	0.0891	0.761	4.824
	15	0.2	1.7881	0.0881	0.766	3.647
Adaptively structured	26	0.2	1.7886	0.0877	0.795	3.176
	28	0.2	1.7872	0.0861	0.716	1.294
	28	0.167	1.7867	0.0857	0.688	0.824
	31	0.167	1.7889	0.0861	0.811	1.294
	32	0.167	1.7869	0.0859	0.699	1.059
	38	0.143	1.7872	0.0858	0.716	0.941
	38	0.2	1.7872	0.0855	0.716	0.588
	38	0.25	1.7872	0.0855	0.716	0.588
	48	0.2	1.7872	0.0853	0.716	0.353
	48	0.167	1.7873	0.0854	0.721	0.471
Unstructured	8	0.33	1.7281	0.0881	2.615	3.647
	12	0.33	1.766	0.0894	0.479	5.176
	17	0.2	1.752	0.0907	1.268	6.706
	18	0.33	1.7754	0.0843	0.051	0.824
	19	0.33	1.7609	0.0874	0.766	2.824

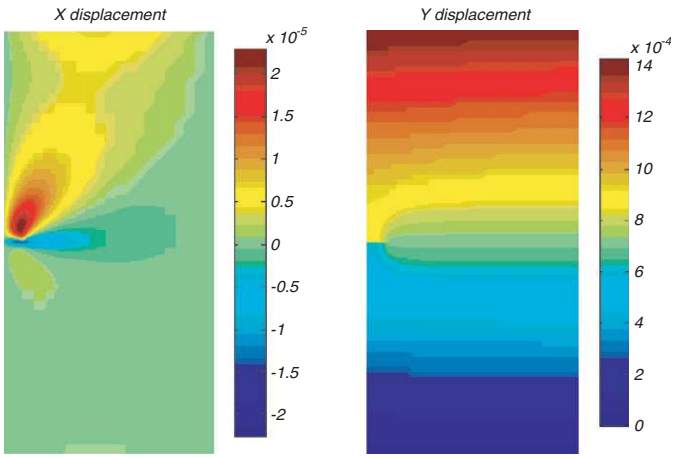

Figure 20. X and Y displacement contours.

Since the loading, material, and geometry are symmetric, only one-half of the plate is considered in the analysis. In Figure 22, traction T_y is applied on the upper and lower boundaries; $\tau_{xy}=0$ on $\overline{AB}$, $T_y=\sigma$ on $\overline{BC}$, $\tau_{xy}=0$, $u_x=0$ on $\overline{CD}$, and $T_y=\sigma$ on $\overline{DA}$.

Adaptive structured finite element models with different numbers of quadrilateral four-noded elements for different crack lengths ($2a/w=0.2$–0.6) are used in this example. Element sizes are substantially smaller in the vicinity of the crack. Figure 23 illustrates the typical mesh utilized for $2a/w=0.5$.

The same Gauss quadrature rules of Section 4 are used and the relative J integral domain size (r_d) is assumed to be $0.2a$.

DOI: 10.1002/nme

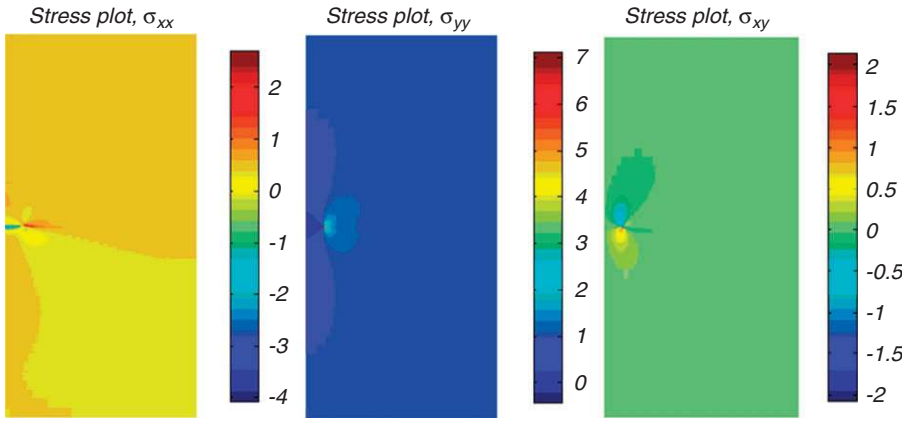

Figure 21. σ_{xx}, σ_{yy}, and σ_{xy} contours.

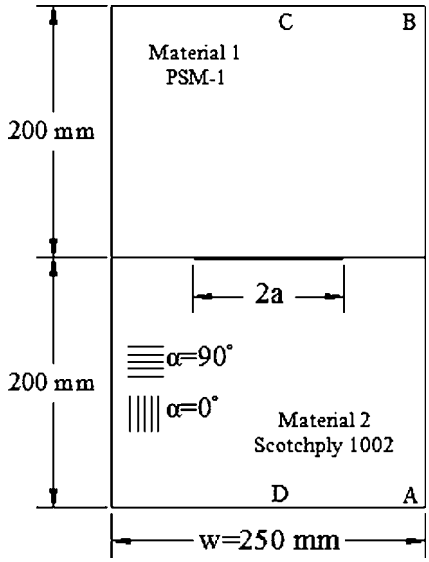

Figure 22. Geometry of a bimaterial plate consisted of isotropic and orthotropic materials.

Table XI. Material properties of the bimaterial constituents.

PSM-1	$E=2.5$ Gpa, $\mu=0.91$ Gpa
Scotch ply 1002	$E_L=39.3$ Gpa, $E_T=9.7$ Gpa, $G_{LT}=3.1$ Gpa, $\nu_{LT}=0.25$

For each crack length and fiber direction in material 2 ($\alpha=0^\circ$ or $\alpha=90^\circ$), the complex stress intensity factors (CSIF) are determined and the normalized amplitude of CSIF is calculated as $|K|/(\sigma\sqrt{\pi a})$, where $|K|=\sqrt{K_1^2+K_2^2}$ and σ is the applied far-field stress. Table XII compares the results of XFEM simulations for different crack lengths based on the new orthotropic enrichment functions. Figure 24 illustrates the normalized CSIFs with respect to the normalized crack lengths for two 0° and 90° fiber orientations.

Shukla *et al.* [73] also performed a study on this problem and evaluated the normalized CSIFs from experiments and boundary collocation method, as depicted in Figure 25. For experimental results, a statistical analysis was performed to obtain the average value and the 95% confidence

DOI: 10.1002/nme

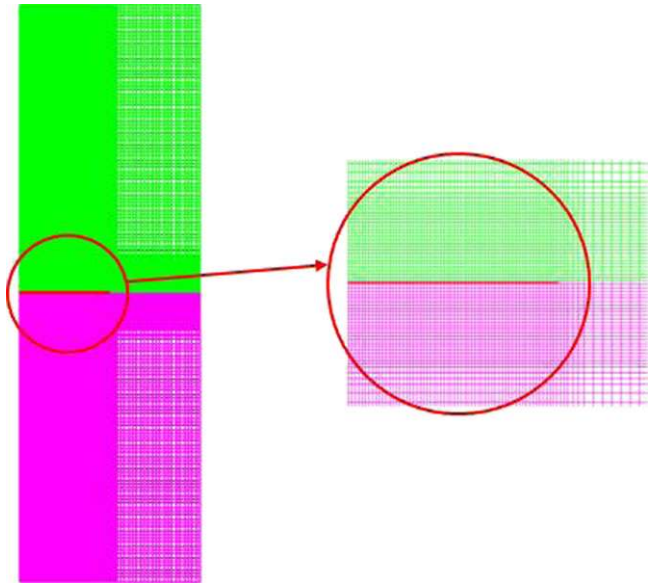

Figure 23. The finite element mesh used for $2a/w=0.5$.

Table XII. Values of normalized amplitude of CSIF for different crack lengths ($|K|/\sigma\sqrt{\pi a}$).

	$2a/w$				
	0.2	0.3	0.4	0.5	0.6
$\alpha=0^\circ$	0.9927	1.0251	1.0734	1.1435	1.2467
$\alpha=90^\circ$	1.0056	1.043	1.0964	1.1701	1.2757

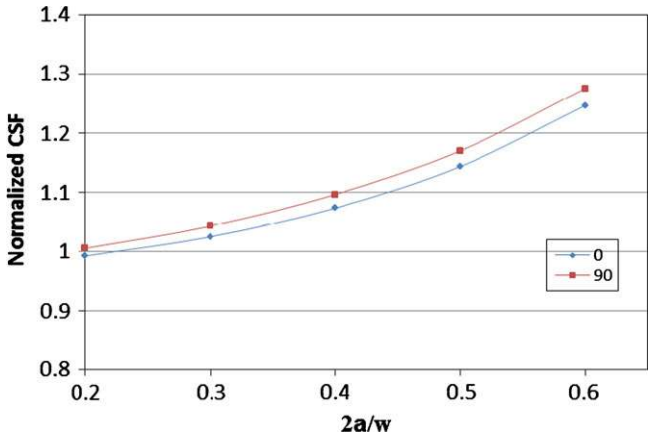

Figure 24. Normalized complex stress intensity factors as a function of normalized crack length.

level. It can be observed that the XFEM numerical estimates of $|K|/(\sigma\sqrt{\pi a})$ are in close agreement with those reported by Shukla *et al.* [73].

Figures 24 and 25 indicate that normalized CSIFs increase as the crack length increases for a given load. Also, for the same crack length, the CSIF values are higher when the fibers are aligned perpendicular to the interface ($\alpha=90^\circ$).

DOI: 10.1002/nme

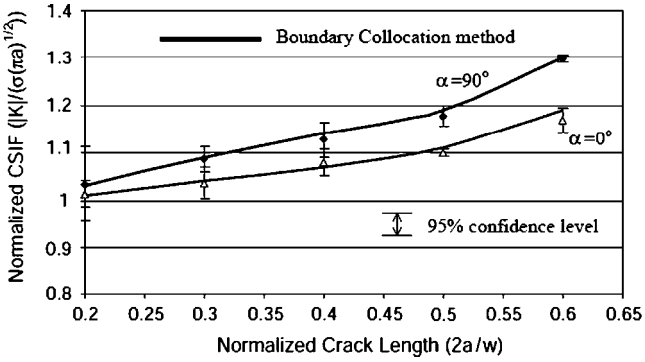

Figure 25. Reference normalized complex stress intensity factors [73].

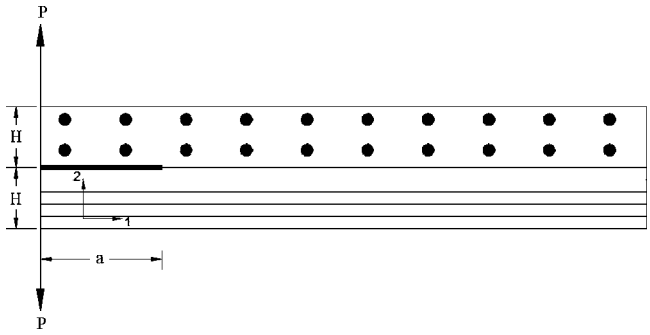

Figure 26. A bilayer orthotropic DCB specimen.

6.5. Orthotropic double cantilever beam

In this example, XFEM is employed to determine the SIFs and the strain energy release rates for interface cracks in a double cantilever beam (DCB) test with orthotropic materials. A bilayer specimen composed of two homogeneous elastic layers, both of thickness H, with a crack length a is considered, as shown in Figure 26. The results of the present simulation are compared with the results reported by Ang *et al.* [74].

In the lower layer, the fiber directions are along the horizontal direction and perpendicular to the applied load P, with E_1 and E_2 as Young's moduli in the first and second principal material axes; G_{12} as the in-plane shear modulus and v_{12} is the Poisson ratio. The fiber direction is along the out of plane direction in the top layer and it is treated as isotropic inplane with E_2 and v_{12} as Young's modulus and the Poisson ratio, respectively. The mechanical properties of the bottom layer are defined in terms of two parameters η_1 and η_2, which are related to the purely imaginary roots of the characteristic equation of the orthotropic material as: [74]

$$\eta_1\eta_2=\left(\frac{E_1}{E_2}\right)^{\frac{1}{2}},\quad \eta_1+\eta_2=\sqrt{2\left[\left(\frac{E_1}{E_2}\right)^{\frac{1}{2}}+\frac{E_1}{2G_{12}}-v_{12}\right]} \tag{54}$$

In numerical models, the relative crack sizes are $a/H=2,4,6$ and these cases of material properties combinations are examined:

Case 1: $\eta_1=0.8, \eta_2=2$;
Case 2: $\eta_1=1, \eta_2=2$;
Case 3: $\eta_1=0.8, \eta_2=3$.

DOI: 10.1002/nme

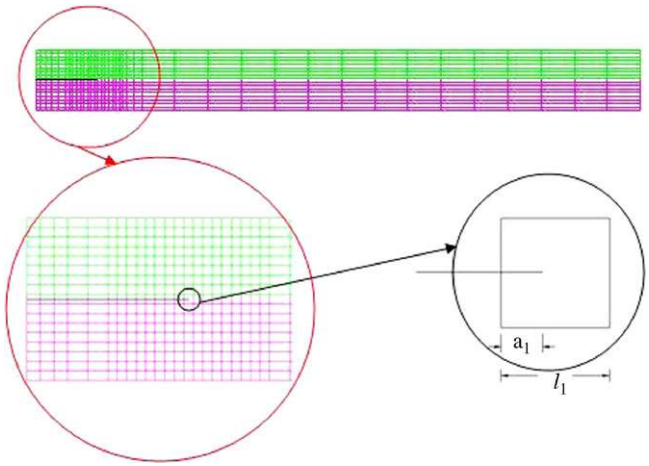

Figure 27. FEM discretization of orthotropic DCB problem.

Table XIII. Comparison of the values of normalized strain energy release rates for different crack lengths, obtained from XFEM and the boundary element method (cases 1 and 2).

	$\frac{a}{H}$	$\frac{r_d}{a}$	$\frac{G}{G_0}$ (XFEM)	$\frac{G}{G_0}$ (BEM) [74]
$\eta_1=0.8$ $\eta_2=2$	2	0.33	3.2996	3.35
	4	0.17	2.4768	2.5
	6	0.125	2.2313	2.2
$\eta_1=1$ $\eta_2=2$	2	0.33	4.5160	4.6
	4	0.17	3.4189	3.3
	6	0.125	3.0931	3.0

The strain energy release rates are computed for each numerical model using the SIFs [26]:

$$G=\frac{1}{4\cosh^2(\pi\varepsilon)}[D_{22}K_1^2+D_{11}K_2^2+2D_{12}K_1^2K_2^2] \tag{55}$$

K_1 and K_2 are the mode I and II SIFs and

$$D=L_{\#1}^{-1}+L_{\#2}^{-1} \tag{56}$$

where L is the Barnett and Lothe tensor, defined in (47).

The reference results for strain energy release rates were normalized using G_0:

$$G_0=\frac{12P^2a^2}{E_1H^3} \tag{57}$$

Adaptive structured finite element models, depicted in Figure 27, with 663 elements and 720 nodes, are employed for different crack lengths. The same Gauss quadrature rules as in Section 4 are used with different relative J integral domain sizes (r_d).

Tables XIII and XIV compare the results of normalized strain energy release rates obtained by the present XFEM models and the values reported by Ang *et al.* [74], which were based on the BEM. Similar results, obtained by Ang *et al.* [74], are illustrated in Figures 28 and 29, where the results of present XFEM simulations are marked by large circles. Very close agreements are observed between the XFEM and reference results.

In order to determine the effect of ratio of crack length in a tip element to the element length (a_1/l_1 in Figure 27), several analyses have been performed on the case 3 model ($\eta_1=0.8, \eta_2=3$), with $r_d/a=0.33$. Table XV shows the results of normalized strain energy release rates for XFEM models and the results reported by Ang *et al.* [74]. The results clearly indicate that the ratio of

DOI: 10.1002/nme

Table XIV. Comparison of the values of normalized strain energy release rates for different crack lengths, obtained from XFEM and the boundary element method (case 3: $\eta_1 = 0.8$ and $\eta_2 = 3$).

$\frac{a}{H}$	$\frac{r_d}{a}$	$\frac{G}{G_0}$ (XFEM)	$\frac{G}{G_0}$ (BEM) [74]
2	0.33	6.1678	6.35
4	0.17	4.6465	4.7
6	0.125	4.1986	4.15

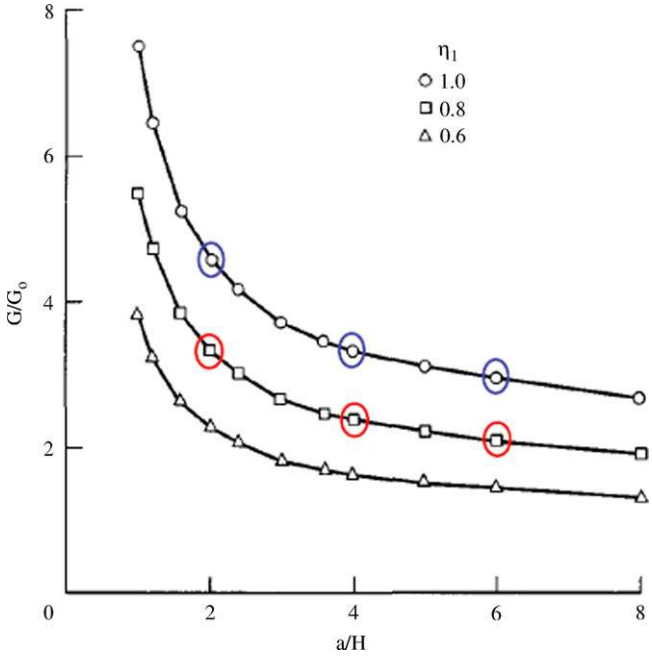

Figure 28. Variations of G/G_0 with a/H for the DCB specimen ($\eta_2 = 2$) using boundary element method [74], compared with XFEM results (large circles).

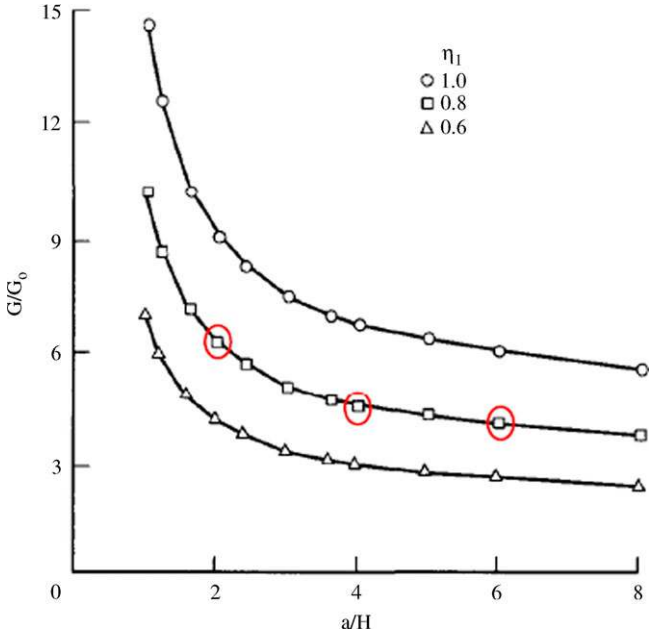

Figure 29. Variation of G/G_0 with a/H for the DCB specimen ($\eta_2 = 3$) using the boundary element method [74], compared with the XFEM results (large circles).

DOI: 10.1002/nme

Table XV. Values of normalized strain energy release rates, using different ratios of crack length in tip element to the length of tip element (case 3: $\eta_1 = 0.8$ and $\eta_2 = 3$).

Crack length in tip element/tip element length (a_1/l_1)	$\frac{G}{G_0}$ (XFEM)	$\frac{G}{G_0}$ (BEM) [74]
0.052	6.1791	6.35
0.28	6.1486	6.35
0.5	6.1678	6.35
0.556	6.1901	6.35
0.811	6.1321	6.35

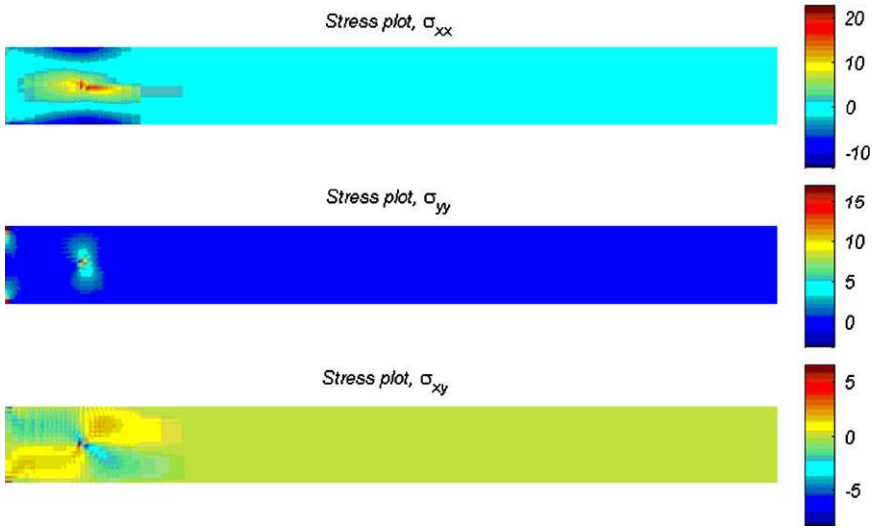

Figure 30. Stress contours of DCB.

crack length in the tip element to the size of tip element does not have a major effect on the results.

Figure 30 illustrates the stress contours of the beam, which clearly indicates the singularity of stress field around the interlaminar crack tip.

7. CONCLUSIONS

The problem of cracks that lie at the interface of two elastically homogeneous orthotropic materials has been studied. The XFEM has been adopted for modeling the interface crack and analyzing the domain numerically. New bimaterial orthotropic crack-tip enrichment functions are extracted from the analytical solution in the vicinity of interfacial crack-tips. The heaviside function, the new near-tip enrichment functions, and the weak discontinuity enrichment functions have been implemented in the XFEM to simulate the interface crack between two orthotropic composite layers. Mixed-mode SIFs and energy release rates for bimaterial interfacial cracks have been numerically evaluated using the domain form of the interaction integral. The obtained results have been compared with the available reference solutions and exhibited close agreement. In addition to the simulation of several crack lengths (as a representation of crack propagation) on a fixed finite element mesh, different types and sizes of mesh and different relative J integral domain sizes have been utilized in order to investigate the robustness of the present method. The proposed bimaterial orthotropic enrichment functions can be degenerated into bimaterial isotropic cases as well as a crack in an isotropic/orthotropic medium, for which simple enrichments are already available.

DOI: 10.1002/nme

The combined set of inplane and interlaminar enrichments is expected to allow for a full fracture analysis of layered orthotropic composites by XFEM in future studies.

APPENDIX A

The general crack-tip stress fields under the mixed mode loading in the upper layer of a cracked bi-material specimen have been obtained by Lee [28]:

$$\sigma_x = \frac{K_{\mathrm{I}}}{2\sqrt{2\pi}D\cosh(\varepsilon\pi)}\left[-p^2\left\{e^{\varepsilon(\pi-\theta_l)}\bar{A}\cos\left(\varepsilon\ln(r_l)-\frac{\theta_l}{2}\right)+e^{-\varepsilon(\pi-\theta_l)}A\cos\left(\varepsilon\ln(r_l)+\frac{\theta_l}{2}\right)\right\}\right.$$
$$\times(r_l)^{\frac{-1}{2}}+q^2\left\{e^{\varepsilon(\pi-\theta_s)}\bar{B}\cos\left(\varepsilon\ln(r_s)-\frac{\theta_s}{2}\right)+e^{-\varepsilon(\pi-\theta_s)}B\cos\left(\varepsilon\ln(r_s)+\frac{\theta_s}{2}\right)\right\}(r_s)^{\frac{-1}{2}}\Big]$$
$$+\frac{K_{\mathrm{II}}}{2\sqrt{2\pi}D\cosh(\varepsilon\pi)}\left[p^2\left\{e^{\varepsilon(\pi-\theta_l)}\bar{A}\sin\left(\varepsilon\ln(r_l)-\frac{\theta_l}{2}\right)+e^{-\varepsilon(\pi-\theta_l)}A\sin\left(\varepsilon\ln(r_l)+\frac{\theta_l}{2}\right)\right\}\right.$$
$$\times(r_l)^{\frac{-1}{2}}-q^2\left\{e^{\varepsilon(\pi-\theta_s)}\bar{B}\sin\left(\varepsilon\ln(r_s)-\frac{\theta_s}{2}\right)+e^{-\varepsilon(\pi-\theta_s)}B\sin\left(\varepsilon\ln(r_s)+\frac{\theta_s}{2}\right)\right\}(r_s)^{\frac{-1}{2}}\Big] \quad \text{(A1)}$$

$$\sigma_y = \frac{K_{\mathrm{I}}}{2\sqrt{2\pi}D\cosh(\varepsilon\pi)}\left[\left\{e^{\varepsilon(\pi-\theta_l)}\bar{A}\cos\left(\varepsilon\ln(r_l)-\frac{\theta_l}{2}\right)+e^{-\varepsilon(\pi-\theta_l)}A\cos\left(\varepsilon\ln(r_l)+\frac{\theta_l}{2}\right)\right\}\right.$$
$$\times(r_l)^{\frac{-1}{2}}-\left\{e^{\varepsilon(\pi-\theta_s)}\bar{B}\cos\left(\varepsilon\ln(r_s)-\frac{\theta_s}{2}\right)+e^{-\varepsilon(\pi-\theta_s)}B\cos\left(\varepsilon\ln(r_s)+\frac{\theta_s}{2}\right)\right\}(r_s)^{\frac{-1}{2}}\Big]$$
$$+\frac{K_{\mathrm{II}}}{2\sqrt{2\pi}D\cosh(\varepsilon\pi)}\left[\left\{-e^{\varepsilon(\pi-\theta_l)}\bar{A}\sin\left(\varepsilon\ln(r_l)-\frac{\theta_l}{2}\right)-e^{-\varepsilon(\pi-\theta_l)}A\sin\left(\varepsilon\ln(r_l)+\frac{\theta_l}{2}\right)\right\}\right.$$
$$\times(r_l)^{\frac{-1}{2}}+\left\{e^{\varepsilon(\pi-\theta_s)}\bar{B}\sin\left(\varepsilon\ln(r_s)-\frac{\theta_s}{2}\right)+e^{-\varepsilon(\pi-\theta_s)}B\sin\left(\varepsilon\ln(r_s)+\frac{\theta_s}{2}\right)\right\}(r_s)^{\frac{-1}{2}}\Big] \quad \text{(A2)}$$

$$\tau_{xy} = \frac{K_{\mathrm{I}}}{2\sqrt{2\pi}D\cosh(\varepsilon\pi)}\left[\alpha_l\left\{e^{\varepsilon(\pi-\theta_l)}\bar{A}\sin\left(\varepsilon\ln(r_l)-\frac{\theta_l}{2}\right)-e^{-\varepsilon(\pi-\theta_l)}A\sin\left(\varepsilon\ln(r_l)+\frac{\theta_l}{2}\right)\right\}(r_l)^{\frac{-1}{2}}\right.$$
$$+\alpha_s\left\{-e^{\varepsilon(\pi-\theta_s)}\bar{B}\sin\left(\varepsilon\ln(r_s)-\frac{\theta_s}{2}\right)+e^{-\varepsilon(\pi-\theta_s)}B\sin\left(\varepsilon\ln(r_s)+\frac{\theta_s}{2}\right)\right\}(r_s)^{\frac{-1}{2}}\Big]$$
$$+\frac{K_{\mathrm{II}}}{2\sqrt{2\pi}D\cosh(\varepsilon\pi)}\left[\alpha_l\left\{e^{\varepsilon(\pi-\theta_l)}\bar{A}\cos\left(\varepsilon\ln(r_l)-\frac{\theta_l}{2}\right)-e^{-\varepsilon(\pi-\theta_l)}A\cos\left(\varepsilon\ln(r_l)+\frac{\theta_l}{2}\right)\right\}\right.$$
$$\times(r_l)^{\frac{-1}{2}}+\alpha_s\left\{-e^{\varepsilon(\pi-\theta_s)}\bar{B}\cos\left(\varepsilon\ln(r_s)-\frac{\theta_s}{2}\right)+e^{-\varepsilon(\pi-\theta_s)}B\cos\left(\varepsilon\ln(r_s)+\frac{\theta_s}{2}\right)\right\}(r_s)^{\frac{-1}{2}}\Big] \quad \text{(A3)}$$

and the associated displacement fields are:

$$u_x = \frac{K_{\mathrm{I}}}{\sqrt{2\pi}\left(1+4\varepsilon^2\right)D\cosh(\varepsilon\pi)}\left\{e^{\varepsilon(\pi-\theta_l)}p_l\bar{A}\left[\cos\left(\varepsilon\ln(r_l)-\frac{\theta_l}{2}\right)+2\varepsilon\sin\left(\varepsilon\ln(r_l)+\frac{\theta_l}{2}\right)\right]\right.$$
$$\times(r_l)^{\frac{1}{2}}+e^{-\varepsilon(\pi-\theta_l)}p_lA\left[\cos\left(\varepsilon\ln(r_l)-\frac{\theta_l}{2}\right)+2\varepsilon\sin\left(\varepsilon\ln(r_l)-\frac{\theta_l}{2}\right)\right](r_l)^{\frac{1}{2}}\Big]$$

DOI: 10.1002/nme

$$
\begin{aligned}
&-\mathrm{e}^{\varepsilon(\pi-\theta_s)}p_s\bar{B}\left[\cos\left(\varepsilon\ln(r_s)+\frac{\theta_s}{2}\right)+2\varepsilon\sin\left(\varepsilon\ln(r_s)+\frac{\theta_s}{2}\right)\right](r_s)^{\frac{1}{2}}\\
&-\mathrm{e}^{-\varepsilon(\pi-\theta_s)}p_sB\left[\cos\left(\varepsilon\ln(r_s)-\frac{\theta_s}{2}\right)+2\varepsilon\sin\left(\varepsilon\ln(r_s)-\frac{\theta_s}{2}\right)\right](r_s)^{\frac{1}{2}}\Bigg]\Bigg\}\\
&+\frac{K_{\mathrm{II}}}{\sqrt{2\pi}\left(1+4\varepsilon^2\right)D\cosh(\varepsilon\pi)}\Bigg\{-\mathrm{e}^{\varepsilon(\pi-\theta_l)}p_l\bar{A}\left[\sin\left(\varepsilon\ln(r_l)+\frac{\theta_l}{2}\right)-2\varepsilon\cos\left(\varepsilon\ln(r_l)+\frac{\theta_l}{2}\right)\right]\\
&(r_l)^{\frac{1}{2}}-\mathrm{e}^{-\varepsilon(\pi-\theta_l)}p_lA\left[\sin\left(\varepsilon\ln(r_l)-\frac{\theta_l}{2}\right)-2\varepsilon\cos\left(\varepsilon\ln(r_l)-\frac{\theta_l}{2}\right)\right](r_l)^{\frac{1}{2}}\Bigg]\\
&+\mathrm{e}^{\varepsilon(\pi-\theta_s)}p_s\bar{B}\left[\sin\left(\varepsilon\ln(r_s)+\frac{\theta_s}{2}\right)-2\varepsilon\cos\left(\varepsilon\ln(r_s)+\frac{\theta_s}{2}\right)\right](r_s)^{\frac{1}{2}}\\
&+\mathrm{e}^{-\varepsilon(\pi-\theta_s)}p_sB\left[\sin\left(\varepsilon\ln(r_s)-\frac{\theta_s}{2}\right)-2\varepsilon\cos\left(\varepsilon\ln(r_s)-\frac{\theta_s}{2}\right)\right](r_s)^{\frac{1}{2}}\Bigg]\Bigg\}
\end{aligned}
\tag{A4}
$$

$$
\begin{aligned}
u_y=&\frac{K_{\mathrm{I}}}{\sqrt{2\pi}\left(1+4\varepsilon^2\right)D\cosh(\varepsilon\pi)}\Bigg\{\mathrm{e}^{\varepsilon(\pi-\theta_l)}q_l\bar{A}\left[\sin\left(\varepsilon\ln(r_l)+\frac{\theta_l}{2}\right)-2\varepsilon\cos\left(\varepsilon\ln(r_l)+\frac{\theta_l}{2}\right)\right]\\
&\times(r_l)^{\frac{1}{2}}-\mathrm{e}^{-\varepsilon(\pi-\theta_l)}q_lA\left[\sin\left(\varepsilon\ln(r_l)-\frac{\theta_l}{2}\right)-2\varepsilon\cos\left(\varepsilon\ln(r_l)-\frac{\theta_l}{2}\right)\right](r_l)^{\frac{1}{2}}\Bigg]\\
&-\mathrm{e}^{\varepsilon(\pi-\theta_s)}q_s\bar{B}\left[\sin\left(\varepsilon\ln(r_s)+\frac{\theta_s}{2}\right)-2\varepsilon\cos\left(\varepsilon\ln(r_s)+\frac{\theta_s}{2}\right)\right](r_s)^{\frac{1}{2}}\\
&+\mathrm{e}^{-\varepsilon(\pi-\theta_s)}q_sB\left[\sin\left(\varepsilon\ln(r_s)-\frac{\theta_s}{2}\right)-2\varepsilon\cos\left(\varepsilon\ln(r_s)-\frac{\theta_s}{2}\right)\right](r_s)^{\frac{1}{2}}\Bigg]\Bigg\}\\
&+\frac{K_{\mathrm{II}}}{\sqrt{2\pi}\left(1+4\varepsilon^2\right)D\cosh(\varepsilon\pi)}\Bigg\{\mathrm{e}^{\varepsilon(\pi-\theta_l)}q_l\bar{A}\left[\cos\left(\varepsilon\ln(r_l)+\frac{\theta_l}{2}\right)+2\varepsilon\sin\left(\varepsilon\ln(r_l)+\frac{\theta_l}{2}\right)\right]\\
&\times(r_l)^{\frac{1}{2}}-\mathrm{e}^{-\varepsilon(\pi-\theta_l)}q_lA\left[\cos\left(\varepsilon\ln(r_l)-\frac{\theta_l}{2}\right)+2\varepsilon\sin\left(\varepsilon\ln(r_l)-\frac{\theta_l}{2}\right)\right](r_l)^{\frac{1}{2}}\Bigg]\\
&-\mathrm{e}^{\varepsilon(\pi-\theta_s)}q_s\bar{B}\left[\cos\left(\varepsilon\ln(r_s)+\frac{\theta_s}{2}\right)+2\varepsilon\sin\left(\varepsilon\ln(r_s)+\frac{\theta_s}{2}\right)\right](r_s)^{\frac{1}{2}}\\
&+\mathrm{e}^{-\varepsilon(\pi-\theta_s)}q_sB\left[\cos\left(\varepsilon\ln(r_s)-\frac{\theta_s}{2}\right)+2\varepsilon\sin\left(\varepsilon\ln(r_s)-\frac{\theta_s}{2}\right)\right](r_s)^{\frac{1}{2}}\Bigg]\Bigg\}
\end{aligned}
\tag{A5}
$$

where K_{I} and K_{II} are the mode 1 and 2 SIFs, respectively, and ε is the index of oscillation defined as

$$
\varepsilon=\frac{1}{2\pi}\ln\left(\frac{1-\beta}{1+\beta}\right) \tag{A6}
$$

where β is the second Dundurs parameter [61] given by:

$$
\beta=\frac{h_{11}}{\sqrt{h_{12}h_{21}}} \tag{A7}
$$

$$
\begin{aligned}
h_{11}&=(l_{11})_1-(l_{11})_2\\
h_{21}&=(l_{21})_1+(l_{21})_2\\
h_{12}&==(l_{12})_1+(l_{12})_2
\end{aligned}
\tag{A8}
$$

DOI: 10.1002/nme

and

$$(l_{11})_k = \left\{ \frac{p_s p - p_l q}{q-p} \right\}_k = \left\{ \frac{q_s - q_l}{q-p} \right\}_k,$$
$$(l_{21})_k = \left\{ \frac{q q_l - p q_s}{q-p} \right\}_k, \qquad k=1,2 \tag{A9}$$
$$(l_{12})_k = \left\{ \frac{p_l - p_s}{q-p} \right\}_k,$$

Subscripts $k=1,2$ denote the upper and lower materials, respectively. Also,

$$p_l = -p^2 a_{11} + a_{12}, \quad p_s = -q^2 a_{11} + a_{12} \tag{A10}$$

$$q_l = \frac{-p^2 a_{12} + a_{22}}{p}, \quad q_s = \frac{-q^2 a_{12} + a_{22}}{q} \tag{A11}$$

$$A = q+\eta, \quad \bar{A} = q-\eta, \quad B = p+\eta, \quad \bar{B} = p-\eta, \quad D = [q-p]_k \tag{A12}$$

$$\eta = \left(\frac{h_{21}}{h_{12}} \right)^{\frac{1}{2}} \tag{A13}$$

Variables r_j, θ_j $(j=l,s)$are related to polar coordinate system (r,θ) as:

$$\begin{aligned} r_j &= r\sqrt{\cos^2\theta + Z_j^2 \sin^2\theta}, \\ \theta_j &= \tan^{-1}(Z_j \tan\theta), \end{aligned} \qquad j=l,s, \quad \begin{cases} Z_l = p \\ Z_s = q \end{cases} \tag{A14}$$

In order to obtain the displacement and stress fields in the material below the interface, parameters $\varepsilon\pi$ and $-\varepsilon\pi$ are changed to $-\varepsilon\pi$ and $\varepsilon\pi$, respectively.

These analytical solutions are examined and further discussed in Appendix B for typical bimaterial problems, especially in the limiting cases of crack in dissimilar isotropic layers and similar orthotropic layers (one equivalent orthotropic layer). The main numerical simulations are discussed in Section 6.

APPENDIX B

In this section, analytical solutions are used to discuss the distribution of various stress components in different bimaterial problems. In the limiting case of similar layers, available orthotropic enrichments [41] can be used to verify the new orthotropic bimaterial enrichments.

B.1. Edge crack between two dissimilar orthotropic materials

First, the two layers are assumed to be dissimilar orthotropic materials. In order to illustrate the mixed mode stress fields, the SIFs K_{I} and K_{II} are assumed to be

$$K_{\mathrm{I}} = 10, \quad K_{\mathrm{II}} = 10$$

Materials axes of orthotropy are assumed to be 90° with respect to the x-axis in material 1 and parallel to x-axis in material 2. The crack length is 5 cm, from $(-5,0)$ to $(0,0)$ and the crack-tip is located at $(0,0)$ and the plane stress state is presumed. The following material properties are used: (Norway spruce; Piceaabies) [41]:

$$E_1 = 11.84\,\mathrm{GPa}, \quad E_2 = 0.81\,\mathrm{GPa}, \quad G_{12} = 0.63\,\mathrm{GPa}, \quad \nu_{12} = 0.38$$

DOI: 10.1002/nme

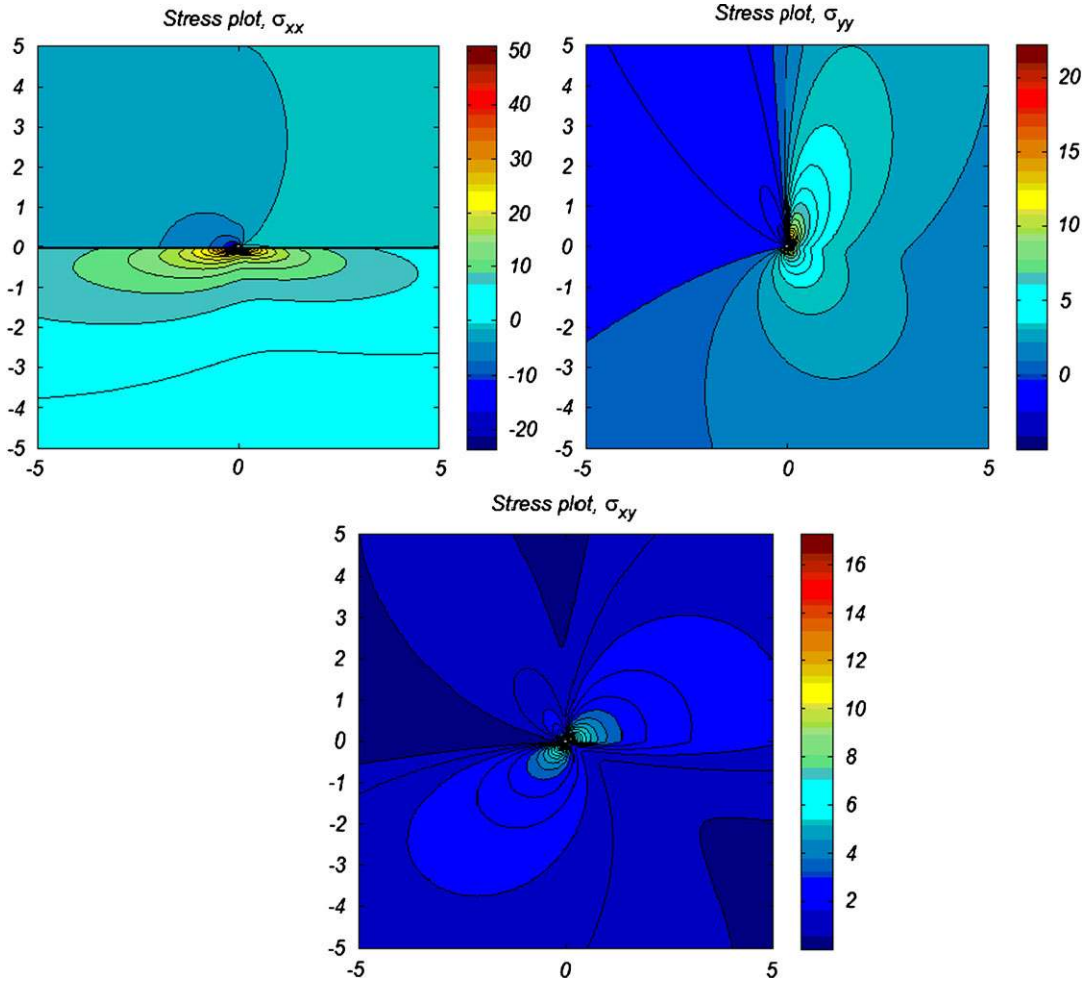

Figure B1. Analytical stress fields for an edge crack between two dissimilar orthotropic materials.

where the 1 and 2 subscripts denote the local material coordinates. The stress fields σ_{xx}, σ_{yy} and σ_{xy} based on Equations (A1)–(A3) for an orthotropic bimaterial interface crack have been plotted in Figure 8. The closest data point to the crack-tip for drawing the contours was at 0.025 cm.

It is clearly observed from Figure B1 that σ_{yy} and σ_{xy} remain zero along the crack length, which identifies a traction-free interfacial crack. Also, σ_{yy} and σ_{xy} are continuous across the interface of two materials that was one of the imposed boundary conditions in obtaining the analytical solutions. σ_{xx} is not continuous along the crack length or across the bimaterial interface.

B.2. Edge crack between two dissimilar isotropic materials

If the two half planes are assumed isotropic, the analytical stress fields can be plotted using the same equations and using isotropic material properties:

Material 1:

$$E_1 = E_2 = 11.84\,\text{GPa}, \quad \nu_{12} = 0.38$$

Material 2:

$$E_1 = E_2 = 15.84\,\text{GPa}, \quad \nu_{12} = 0.45$$

DOI: 10.1002/nme

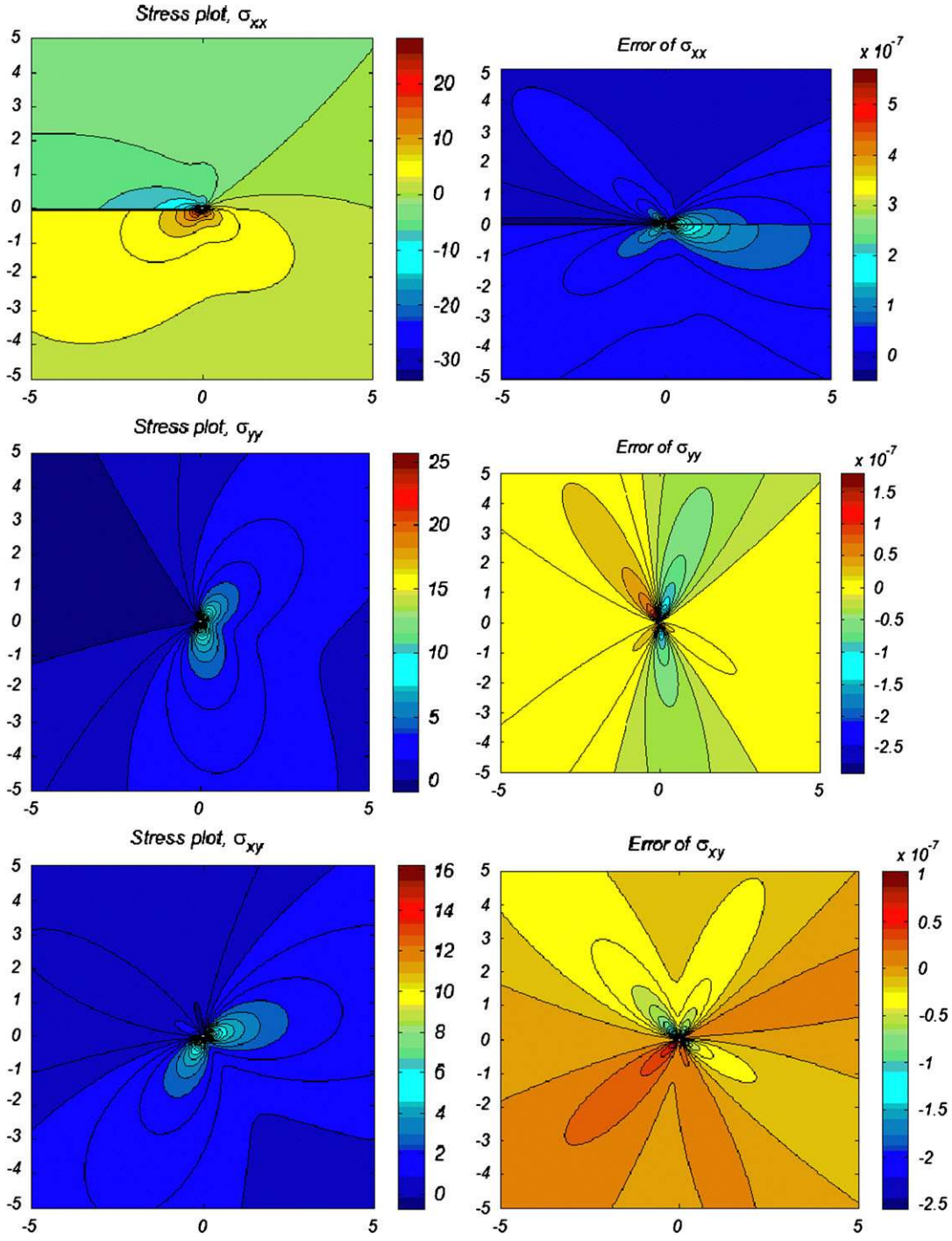

Figure B2. Stress contours and their associated errors with respect to the analytical stress equations in Deng's report [69] for an edge crack between two dissimilar isotropic materials.

The present σ_{xx}, σ_{yy}, and σ_{xy} stress contours (Figure B2) can be verified by comparing them with the analytical stress equations in Deng's report [69], for an isotropic bimaterial interface crack and using the same material properties. Both results are virtually the same, with errors of order 10^{-7}, which proves that the proposed analytical equations for a crack between two orthotropic materials can converge to the already developed analytical solutions for a crack between two isotropic materials.

DOI: 10.1002/nme

It should be noted that if the material properties are chosen to be the same, the analytical equations ((A1)–(A5)) are degenerated into the analytical solutions for a crack in an orthotropic medium, as developed by Asadpoure and Mohammadi [41].

ACKNOWLEDGEMENTS

The authors wish to acknowledge the technical support of the High Performance Computing Lab, of School of Civil Engineering, University of Tehran.

REFERENCES

1. Williams ML. The stress around a fault or crack in dissimilar media. *Bulletin of the Seismological Society of America* 1959; **49**:199–204.
2. England AH. A crack between dissimilar media. *Journal of Applied Mechanics* 1965; **32**:400–402.
3. Erdogan F. Stress distribution in a nonhomogeneous elastic plane with cracks. *Journal of Applied Mechanics* 1963; **30**:232–237.
4. Rice JR, Sih GC. Plane problems of cracks in dissimilar media. *Journal of Applied Mechanics* 1965; **32**:418–423.
5. Malysev BM, Salganik RL. The strength of adhesive joints using the theory of cracks. *International Journal of Fracture* 1965; **1**:114–127.
6. Comninou M. The interface crack. *Journal of Applied Mechanics* 1977; **44**:631–636.
7. Comninou M, Schmuser D. The interface crack in a combined tension-compression and shear field. *Journal of Applied Mechanics* 1979; **46**:345–348.
8. Sun CT, Jih CJ. On strain energy release rate for interfacial cracks in bimaterial media. *Engineering Fracture Mechanics* 1987; **28**:13–20.
9. Hutchinson JW, Mear M, Rice JR. Crack paralleling in between dissimilar materials. *Journal of Applied Mechanics* 1987; **54**:828–832.
10. Rice JR. Elastic fracture mechanics concepts for interfacial cracks. *Journal of Applied Mechanics* 1988; **55**:98–103.
11. Gotoh M. Some problems of bonded anisotropic plates with crack along the bond. *International Journal of Fracture* 1967; **3**:253–265.
12. Clements DL. A crack between dissimilar anisotropic media. *International Journal of Engineering Science* 1971; **9**:257–265.
13. Willis JR. Fracture mechanics of interfacial cracks. *Journal of the Mechanics and Physics of Solids* 1971; **19**:353–368.
14. Wang SS, Choi I. The crack between dissimilar anisotropic materials. *Journal of Applied Mechanics* 1983; **50**:169–178.
15. Wang SS, Choi I. The crack between dissimilar anisotropic composites under mixed-mode loading. *Journal of Applied Mechanics* 1983; **50**:179–183.
16. Ting TCT. Explicit solution and invariance of the singularities at a crack in anisotropic composites. *International Journal of Solids and Structures* 1986; **22**:965–983.
17. Tewary VK, Wagoner RH, Hirth JP. Elastic Green's function for a composite solid with a planar interface. *Journal of Materials Research* 1989; **4**:113–136.
18. Bassani JL, Qu J. Finite crack on bimaterial and bicrystals. *Journal of the Mechanics and Physics of Solids* 1989; **37**:435–453.
19. Sun CT, Manoharan MG. Strain energy release rate of an interfacial crack between two orthotropic solids. *Journal of Composite Materials* 1989; **23**:460–478.
20. Wu KC. Stress intensity factor and energy release rate for interfacial cracks between dissimilar anisotropic materials. *Journal of Applied Mechanics* 1990; **57**:882–886.
21. Gao H, Abbudi M, Barnett DM. Interfacial crack-tip field in anisotropic elastic solids. *Journal of Applied Mechanics* 1992; **40**:393–416.
22. Hwu C. Explicit solutions for co-linear crack problems. *International Journal of Solids and Structures* 1993; **3**:301–312.
23. Hwu C. Fracture parameters for the orthotropic bimaterial cracks. *Engineering Fracture Mechanics* 1993; **45**: 89–97.
24. Sou Z. Singularities, interfaces and cracks in dissimilar anisotropic media. *Proceedings of Royal Society*, *London* 1990; **427**:331–358.
25. Qian W, Sun CT. Methods for calculating stress intensity factors for interfacial cracks between two orthotropic solids. *International Journal of Solids and Structures* 1998; **35**:3317–3330.
26. Hemanth D, Shivakumar Aradhya KS, Rama Murthy TS, Govinda Raju N. Strain energy release rates for an interface crack in orthotropic media—a finite element investigation. *Engineering Fracture Mechanics* 2005; **72**:759–772.
27. Yang W, Sou Z, Shih CF. Mechanics of dynamic debonding. *Proceedings of Royal Society*, *London* 1991; **33**:679–697.

DOI: 10.1002/nme

28. Lee KH. Stress and displacement fields for propagating the crack along the interface of dissimilar orthotropic materials under dynamic mode I and II load. *Journal of Applied Mechanics* 2000; **67**:223–228.
29. Mohammadi S. *Extended Finite Element Method*. Wiley/Blackwell Publishing: U.K., 2008.
30. Belytschko T, Black T. Elastic crack growth in finite elements with minimal remeshing. *International Journal for Numerical Methods in Engineering* 1999; **45**:601–620.
31. Moës N, Dolbow J, Belytschko T. A finite element method for crack growth without remeshing. *International Journal for Numerical Methods in Engineering* 1999; **46**:131–150.
32. Sukumar N, Moës N, Moran B, Belytschko T. Extended finite element method for three dimensional crack modelling. *International Journal for Numerical Methods in Engineering* 2000; **48**:1549–1570.
33. Dolbow J, Moës N, Belytschko T. An extended finite element method for modelling crack growth with frictional contact. *Computer Methods in Applied Mechanics and Engineering* 2001; **190**:6825–6846.
34. Mergheim J, Kuh E, Steinmann P. A finite element method for the computational modelling of cohesive cracks. *International Journal for Numerical Methods in Engineering* 2005; **63**:276–289.
35. Belytschko T, Chen H, Xu J, Zi G. Dynamic crack propagation based on loss of hyperbolicity and a new discontinuous enrichment. *International Journal for Numerical Methods in Engineering* 2003; **58**:1873–1905.
36. Belytschko T, Chen H. Singular enrichment finite element method for elastodynamic crack propagation. *International Journal for Numerical Methods in Engineering* 2004; **1**(1):1–15.
37. Rozycki P, Moës N, Béchet E, Dubois C. X-FEM explicit dynamics for constant strain elements to alleviate mesh constraints on internal or external boundaries. *Computer Methods in Applied Mechanics and Engineering* 2008; **197**:349–363.
38. Bechet E, Minnebo H, Moës N, Burgardt B. Improved implementation and robustness study of the X-FEM for stress analysis around cracks. *International Journal for Numerical Methods in Engineering* 2005; **64**:1033–1056.
39. Asadpoure A, Mohammadi S, Vafai A. Crack analysis in orthotropic media using the extended finite element method. *Thin Walled Structures* 2007; **44**(9):1031–1038.
40. Asadpoure A, Mohammadi S, Vafai A. Modeling crack in orthotropic media using coupled finite element and partition of unity methods. *Finite Elements in Analysis and Design* 2006; **42**(13):1165–1175.
41. Asadpoure A, Mohammadi S. Developing new enrichment functions for crack simulation in orthotropic media by the extended finite element method. *International Journal for Numerical Methods in Engineering* 2007; **69**:2150–2172.
42. Motamedi D, Mohammadi S. Dynamic crack propagation analysis of orthotropic media by the extended finite element method. *International Journal of Fracture* 2010; **161**:21–39.
43. Motamedi D, Mohammadi S. Dynamic analysis of fixed cracks in composites by the extended finite element method. *Engineering Fracture Mechanics* 2010; **77**:3373–3393.
44. Motamedi D, Mohammadi S. New dynamic orthotropic enrichment functions for XFEM fracture analysis of composites. 2010; submitted.
45. O'Brien K. Analysis of local delaminations and their influence on composite laminate behavior. In *Delamination and Debonding of Materials*, Johnson WS (ed.). ASTM STP 876. Americal Society for Testing and Material: Philadelphia, 1985; 282–297.
46. Parker AP. *The Mechanics of Fracture and Fatigue*, *An Introduction*. E. & F.N. SPON Ltd.: London, 1981; 89–122.
47. Rowlands RE. Strength (failure) theories and their experimental correlation. In *Handbook of Composites*, *Volume 3—Failure Mechanics of Composites*, Chapter 2, Sih GC, Skudra AM (eds). Elsevier: Amsterdam, 1985; 71–125.
48. Sprenger W, Gruttmann F, Wagner W. Delamination growth analysis in laminated structures with continuum-based 3D-shell elements and a viscoplastic softening model. *Computer Methods in Applied Mechanics and Engineering* 2000; **185**:123–139.
49. Mohammadi S, Moosavi AA. 3D multi delamination/fracture analysis of composites subjected to impact loadings. *Journal of Composite Materials*, *Part B* 2007; **41**(12):1459–1475.
50. Mohammadi S, Forouzan-Sepehr S. 3D adaptive multi fracture analysis of composites. *Materials Science Forum*, *Part B* 2003; **440–441**:145–152.
51. Sukumar N, Huang ZY, Prévost JH, Suo Z. Partition of unity enrichment for bimaterial interface cracks. *International Journal for Numerical Methods in Engineering* 2004; **59**:1075–1102.
52. Hettich T, Ramm E. Interface material failure modeled by the extended finite-element method and level sets. *Computer Methods in Applied Mechanics and Engineering* 2006; **195**:4753–4767.
53. Rammers JJC, Wells GN, de Borst R. A solid-like shell element allowing for arbitrary delaminations. *International Journal for Numerical Methods in Engineering* 2003; **58**:2013–2040.
54. Hettich T, Hund A, Ramm E. Modeling of failure in composites by X-FEM and level sets within a multiscale framework. *Computer Methods in Applied Mechanics and Engineering* 2008; **197**:414–424.
55. Nagashima T, Suemasu H. Application of extended finite element method to fracture of composite materials. *European Congress on Computational Methods in Applied Sciences and Engineering* (*ECCOMAS*), Jyväskylä, Finland, 2004.
56. Nagashima T, Suemasu H. Stress analysis of composite laminates with delamination using XFEM. *International Journal of Computational Methods* 2006; **3**:521–543.

DOI: 10.1002/nme

57. Esna Ashari S, Mohammadi S. XFEM delamination analysis of composite laminates by new orthotropic enrichment functions. *Proceedings of First International Conference on Extended Finite Element Method* (*XFEM2009*), Aachen, Germany, 2009.
58. Esna Ashari S, Mohammadi S. Modeling delamination in composite laminates using XFEM by new orthotropic enrichment functions. *WCCM/APCOM 2010*, Sydney, Australia. *IOP Conference Series*: *Materials Science and Engineering* 2010; **10**:012240.
59. Lekhnitskii SG. *Theory of an Anisotropic Elastic Body*. Holden-Day: San Francisco, 1963.
60. Lee KH, Hawong JS, Choi SH. Dynamic stress intensity factors K_I and K_{II} and dynamic crack propagating characteristics of orthotropic materials. *Engineering Fracture Mechanics* 1996; **53**:119–140.
61. Dundurs J. Edge-bonded dissimilar orthogonal elastic wedges. *Journal of Applied Mechanics* 1969; **36**:650–652.
62. Bordas S, Legay A. *X-FEM Mini-course*. EPFL: Lausanne, Switzerland, 2005.
63. Moës N, Cloirec M, Cartraud P, Remacle JF. A computational approach to handle complex microstructure geometries. *Computer Methods in Applied Mechanics and Engineering* 2003; **192**:3163–3177.
64. Chow WT, Boem HG, Alturi SN. Calculation of stress intensity factors for interfacial crack between dissimilar anisotropic media using a hybrid element method and the mutual integral. *Computational Mechanics* 1995; **15**:546–557.
65. Li FZ, Shih CF, Needleman A. A comparison of methods for calculating energy release rates. *Engineering Fracture Mechanics* 1985; **21**:405–421.
66. Sih GC, Paris P, Irwin G. On cracks in rectilinearly anisotropic bodies. *International Journal of Fracture Mechanics* 1965; **1**(3):189–203.
67. Barnett DM, Lothe J. Synthesis of the sextic and the integral formalism for dislocation, Green's function and surface waves in anisotropic elastic solids. *Physica Norvegica* 1973; **7**:13–19.
68. Dongye C, Ting TCT. Explicit expressions of Barnett–Lothe tensors and their associated tensors for orthotropic materials. *Quarterly of Applied Mathematics* 1989; **47**:732–734.
69. Deng X. Mechanics of debonding and delamination in composites: asymptotic studies. *Composites Engineering* 1995; **5**:1299–1315.
70. Kim JH, Paulino GH. The interaction integral for fracture of orthotropic functionally graded materials: evaluation of stress intensity factors. *International Journal of Solids and Structures* 2003; **40**:3967–4001.
71. Qu J, Bassani JL. Interfacial fracture mechanics for anisotropic bimaterials. *Journal of Applied Mechanics* 1993; **60**:422–431.
72. Chow WT, Atluri SN. Stress Intensity factors as the fracture parameters for delamination crack growth in composite laminates. *Computational Mechanics* 1998; **21**:1–10.
73. Shukla A, Chalivendra VB, Parameswran V, Lee KH. Photoelastic investigation of fracture between orthotropic and isotropic materials. *Optic and Lasers in Engineering* 2003; **40**:307–324.
74. Ang HE, Torrance JE, Tan CL. Boundary element analysis of orthotropic delamination specimens with interface cracks. *Engineering Fracture Mechanics* 1996; **54**:601–615.

DOI: 10.1002/nme